Karlova Univerzita v Praze

Matematicko-fyzikální fakulta

BAKALÁŘSKÁ PRÁCE

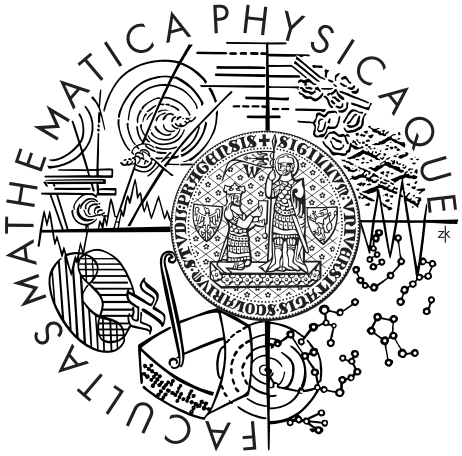

Lukáš Kripner

MHD nestability plazmatu pozorované ve výbojích tokamaku COMPASS

Katedra povrchů a plazmatu,

Ústav fyziky plazmatu AV ČR, v.v.i.

Vedoucí: prof. RNDr. Zdeněk Němeček, DrSc.

Vedoucí-specialista: Mgr. Vladimír Weinzettl, Ph.D.

Studijní program: Fyzika

Studijní obor: Obecná fyzika

Praha, 2013

Charles University in Prague

Faculty of Mathematics and Physics

BACHELOR THESIS

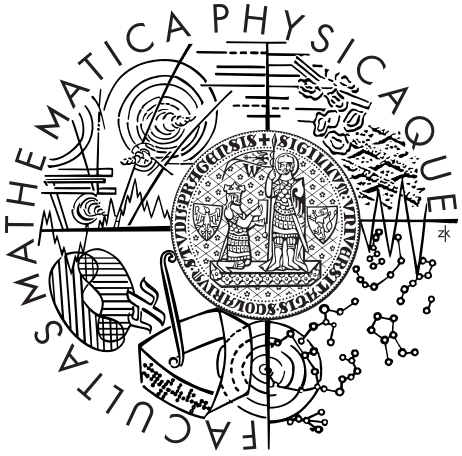

Lukáš Kripner

MHD Plasma Instabilities Observed in Discharges of the COMPASS Tokamak

Department of Surface and Plasma Science,

Institute of Plasma Physics AS CR, v.v.i.

Supervisor: prof. RNDr. Zdeněk Němeček, DrSc.

Supervisor-specialist: Mgr. Vladimír Weinzettl, Ph.D.

Study programme: Physics

Specialization: General Physics

Prague, 2013

Na tomto místě bych velice rád poděkoval všem, kteří mi s prací pomohli, nebo alespoň byly s to mě snášet v posledních dnech před odevzdáním práce.

Na prvním místě musím poděkovat oběma mým vedoucím za neocenitelnou pomoc, trpělivost, spoustu času a vlídnost. Mé díky patří také mému bratrovi, Janu Veselému, a jeho ženě, Jitce Veselé, za pomoc při řešení logistických problémů vzniklých při samotném završování práce. V neposlední řadě bych chtěl vyjádřit vděk mým kolegům na oddělení tokamaku, jmenovitě Ing. Martinu Imríškovi a Mgr. Josefu Havlíčkovi za cenné rady a ochotu. Cennými radami a ochotou také přispěla prof. RNDr. Jana Šafranková, DrSc., proto i jí zde skládám poklonu.

I declare that I carried out this bachelor thesis independently, and only with the cited sources, literature and other professional sources.

I understand that my work relates to the rights and obligations under the Act No. 121/2000 Coll., the Copyright Act, as amended, in particular the fact that the Charles University in Prague has the right to conclude a license agreement on the use of this work as a school work pursuant to Section 60 paragraph 1 of the Copyright Act.

In Prague date 26th of June, 2013 Lukáš Kripner

Název práce: MHD nestability plazmatu pozorované ve výbojích tokamaku COMPASS

Autor: Lukáš Kripner

Katedra: Katedra fyziky povrchů a plazmatu

Vedoucí bakalářské práce: prof. RNDr. Zdeněk Němeček, DrSc.

Vedoucí-specialista: Mgr. Vladimir Weinzettl, Ph.D., UFP AV ČR, v.v.i.

Abstrakt: Tokamak Compass ($R = 0.56\,\mathrm{m}$, $a = (0.23 \times 0.38)\,\mathrm{m}$, $I_p = 200 - 400\,\mathrm{kA}$, $B_T = 1.2 - 2.1\,\mathrm{T}$ a délkou pulsu přes 1 s) je nejmenší zařízení s ITER-relevantní geometrií plazmatu v poměru 1:10 k velikosti ITERu.
Udržení tokamakového plazmatu je silně omezeno výskytem magnetohydrodynamických (MHD) nestabilit, které se vyskytují během výboje. Na základě rešerše literatury jsou v práci shrnuty teoretické úvahy a typické chování MHD nestabilit tokamakového plazmatu. Toto pojednání je zakončeno přehledem diagnostiky tokamaku Compass a různých technik určených na analýzu dat. Na závěr jsou ukázány a diskutovány ukázky chování plazmatu na tokamaku Compass ovlivněného tearing módy a sawtooth.

Klíčová slova: MHD, tearing mody, sawtooth, analýza dat, diagnostika

Title: MHD plasma instabilities observed in discharges of the COMPASS tokamak

Author: Lukáš Kripner

Department: Department of Surface and Plasma Science

Supervisor: prof. RNDr. Zdeněk Němeček, DrSc.

Supervisor-specialist: Mgr. Vladimir Weinzettl, Ph.D., IPP ASCR, v.v.i.

Abstract: Compass tokamak ($R = 0.56\,\mathrm{m}$, $a = (0.23 \times 0.38)\,\mathrm{m}$, $I_p = 200 - 400\,\mathrm{kA}$, $B_T = 1.2 - 2.1\,\mathrm{T}$ and pulse length up to 1 s) is the smallest device with ITER-relevant plasma geometry with scale 1:10 to the ITER size.
A tokamak plasma confinement is strongly limited by an occurrence of magnetohydrodynamic (MHD) instabilities occurring during the discharge. In the thesis, theoretical considerations and a typical behaviour of the tokamak plasma MHD instabilites are summarized based on the literature overview. This discussion is complemented with an overview of the Compass diagnostics and different data analysis techniques. Finally, the examples of the Compass plasma behaviour influenced by sawtooth instability and tearing modes are shown and discussed.

Keywords: MHD, tearing modes, sawtooth, data analysis, diagnostics

Contents

Introduction

Energetic entitlements of a society are permanently increasing. According to some estimations (Freidberg [2007]), the current world supplies of coal will last for about 200 years. They will last for about 900 years in combination with other fuels. Supplies of uranium 235 are estimated only on 20 years and on next 300 years in combinations with other resources. Introduced estimations are based on current consumptions of energetic resources; however, the consumptions are permanently increasing and renewable resources are not capable to cover the whole energy production. From the stated information the need of a new energy resource follows .

Such a source of energy could be a thermonuclear fusion, which needs only isotopes of hydrogen. According to some estimations the world supplies of deuterium stored in oceans will last for next 20,000 years. Tritium might be obtained by fusion itself or by reaction of neutron with lithium. Thus, the fusion energy has potential to cover the world demand for energy. In addition, in contrast with coal or nuclear power plants, fusion power plants are not an ecological threat.

In contrary to nuclear fission, nuclear synthesis happens during the thermonuclear fusion. Light elements are being fused into heavier elements. In the first generation of fusion power plants there will be run a D-T reaction

$$\mathrm{D} + \mathrm{T} \rightarrow {}^{4}\mathrm{He}\,(3.5\,\mathrm{MeV}) + \mathrm{n}\,(14.1\,\mathrm{MeV}), \tag{1}$$

$$\mathrm{n} + {}^{6}\mathrm{Li} \rightarrow {}^{4}\mathrm{He}\,(2.1\,\mathrm{MeV}) + \mathrm{T}\,(3.4\,\mathrm{MeV}) \tag{2}$$

and the tritium will be produced in the walls of the power plant. In the second generation of fusion power plant there will be run a D-D reactions which works only with deuterium are expected:

$$\mathrm{D} + \mathrm{D} \rightarrow \mathrm{T}\,(1\,\mathrm{MeV}) + \mathrm{p}\,(3\,\mathrm{MeV}), \tag{3}$$

$$\mathrm{D} + \mathrm{D} \rightarrow {}^{3}\mathrm{He}\,(0.8\,\mathrm{MeV}) + \mathrm{n}\,(2.5\,\mathrm{MeV}). \tag{4}$$

Unfortunately, it is much harder to reach the second reaction, which solves the problem of the tritium production.

A very promising facility for thermonuclear reactions seems to be a tokamak device. The tokamak is a toroidal device in which the hot plasma is confined by

a magnetic field. At present, works on ITER[1] tokamak are finishing. It should be the first device having a positive energy balance. Therefore, the energy gained from the thermonuclear fusion will exceed the energy needed for susteining of the discharge.

Ignition condition is a very important parameter of a tokamak. This condition is usually called the *Lawson criterion*

$$nT\tau_E > 3 \times 10^{21}\,\mathrm{m}^{-3}\,\mathrm{keV\,s}, \tag{5}$$

where n is plasma density, T plasma temperature and τ_E is confinement time. Very important parameter of Lawson criterion is a confinement time. The most of parameters affecting τ_E reached their current maxima. One from the free parameters is a size of the vacuum vessel, which should be as big as possible to maximize confinement time. Thus, tokamak devices are built such huge.

The plasma confinement is strongly influenced by plasma instabilities. These instabilities can be usually described by a single-fluid magnetohydrodynamic (MHD).

The first chapter of the thesis is dedicated to a brief introduction to tokamak physics. There are summarized basic parameters and equations important to tokamaks and a fusion. The tokamak plasma behaviour is influenced by various drifts and various magnetic field configurations are applied to suppress negative influence of these drifts. A reader is introduced to construction of various magnetic fields on tokamaks. Finally, basic information about Compass tokamak is presented in the chapter.

An overview of the Compass diagnostics is given in the second chapter of the thesis. The diagnostics used during the measurements are then discussed in details, namely, magnetic and soft X-ray diagnostics. The data obtained from these diagnostics can be evaluated by various mathematical techniques, and the important techniques for this thesis are described in the third chapter.

Final two chapters focus on MHD, MHD instabilities and their observations. In the fourth chapter a general introduction to MHD is given and it is accompanied by some theoretical predictions. This chapter is important to a basic

[1] http://www.iter.org/

understanding of a plasma behaviour, thus the section introducing magnetic reconnection significant for creation of tearing modes is presented in this chapter. Next section introduces Grad–Shafranov equation and EFIT tool for reconstruction of various plasma profiles.

The final chapter is concentrated on theory and observations of MHD instabilities. Introduced theories and usually observed plasma behavior is described based on various publications and articles. Substantial part of this chapter is focused on sawtooth instability and later on tearing mode instability. The tearing modes are analysed and also analysis of typical plasma behaviour is done.

Aims of the thesis

As it has been noted in the introduction part, the tokamak plasma confinement is affected by various MHD instabilities, thus the main aim of the thesis is to review the present theories and observations. This goal can be divided into few particular tasks as it follows:

- Introduction to the theory and observations of MHD instabilities.
- Demonstration of different diagnostics available on the Compass tokamak focused mainly on the techniques appropriate for tracking MHD activities.
- Analysis of sawtooth[2] and tearing mode[3] instabilities using various methods of data processing.
- Discussion of examples of the typical tokamak plasma behaviour under various conditions.

[2]See Sec. 5.2.
[3]See Sec. 5.3.

1. Introduction to tokamak physics

A tokamak device uses a toroidal magnetic field to confine a plasma. The hot plasma is in the tokamak vessel confined during so call discharge. The length of discharge is influenced by its quality of confinement. Naturally, it is important to reach the high confinement.

1.1 Beta

The efficiency of plasma confinement can be represented by a ratio of the plasma and magnetic pressures β. In the simplest way, the ratio can be expressed by

$$\beta = \frac{\mu_0 p}{B^2}, \tag{1.1}$$

where μ_0 is permeability of vacuum, p plasma pressure and B magnetic field.

The plasma is confined by the magnetic field, thus the plasma with lower β has a longer confinement time.

Precise calculations supported with tokamak experiments have shown a linear dependence of β on $I_\phi/(aB_\phi)$, where I_ϕ is a plasma current, a minor radius of the tokamak and B_ϕ toroidal magnetic field. Thus, from the scaling reasons, the *normalized beta* β_N has been defined as (Wesson et al. [2004]):

$$\beta_N = \beta[\%]\frac{a[\mathrm{m}]B_\phi[\mathrm{T}]}{I_\phi[\mathrm{MA}]}. \tag{1.2}$$

The approximation of *large aspect-ratio* can be used if the tokamak vessel satisfies the condition

$$\varepsilon = \frac{a}{R} \ll 1, \tag{1.3}$$

where a is a minor radius of the vessel and R is a major tokamak radius (see Fig. 1.1). A large aspect-ratio approximation brings a lot of simplifications.

Apart from β and β_N, *poloidal beta* is for a large aspect-ratio circular plasma (Eq. (1.3)) formulated as

$$\beta_p = \frac{\int p \,\mathrm{d}S}{\mu_0 I^2/8\pi}, \tag{1.4}$$

where the integral is taken over the surface of poloidal cross-section.

1.2 Drifts

A basic behavior of the plasma can be described by various drifts. A lot of construction components of the tokamak are designed to suppress plasma drifts. A derivation of drift equation comes from an idea of the plasma as non-interacting charged particles. The drift equation has a form (Kulhánek [2011])

$$\vec{v}_\perp = \frac{\vec{F}_{ext} \times \vec{B} - \mu \nabla B \times \vec{B} - m\dot{\vec{v}} \times \vec{B}}{QB^2}, \tag{1.5}$$

where $\vec{F}_{ext}$ is some external force affecting particles, Q and m charge and mass of the particle, $\dot{\vec{v}}$ is acceleration of the particle and

$$\mu = \frac{mv_\perp^2}{2B}, \tag{1.6}$$

is *first adiabatic invariant* which remain constant for slowly changing magnetic fields.

$\vec{E} \times \vec{B}$ drift. Charged particle in the electric field $\vec{E}$ is affected by force $\vec{F} = Q\vec{E}$. Thus, Eq. (1.5) gives

$$\vec{v}_E = \frac{\vec{E} \times \vec{B}}{B^2}. \tag{1.7}$$

This drift doesn't depend on mass or charge of the particle. Electrons and ions the in electric field drift with the same velocity.

∇B drift. This drift is determined by the second term in Eq. (1.5) and is caused by gradient of magnitude of the magnetic field. Drift velocity is given by

$$\vec{v}_{\nabla B} = -\frac{\mu \nabla |B| \times \vec{B}}{QB^2} = \frac{mv_\perp^2}{2Q} \frac{\vec{B} \times \nabla |B|}{B^3}. \tag{1.8}$$

This drift is depended on mass and charge of the particle. The drift leads to separation of ions and electrons and thus, constitution of the electric field. Such drift generates $\vec{E} \times \vec{B}$ drift.

Curvature drift. Third term in Eq. (1.5) causes curvature drift. The velocity of this drift is given by

$$\vec{v} = -\frac{m\dot{\vec{v}} \times \vec{B}}{QB^2} = mv_\parallel^2 QB^2 \frac{\vec{R} \times \vec{B}}{R^2}, \tag{1.9}$$

where R is the curvature radius. The curvature drift separates charge and generates the electric field.

Gravitation drift. A particle in the gravitation field is affected by force $\vec{F} = m\vec{g}$. This force leads to the gravitation drift

$$\vec{v}_g = \frac{m\vec{g} \times \vec{B}}{Q\vec{B}^2}. \tag{1.10}$$

This drift also leads to $\vec{E} \times \vec{B}$ drift.

Polarization drift. Time depended electric field leads to force

$$\frac{m}{B^2}\frac{\mathrm{d}\vec{E}}{\mathrm{d}t} \times \vec{B}$$

and polarization drift

$$\vec{v}_P = \frac{m}{QB^4}\frac{\mathrm{d}\vec{E}}{\mathrm{d}t} \times \vec{B}. \tag{1.11}$$

1.3 Introduction to tokamaks

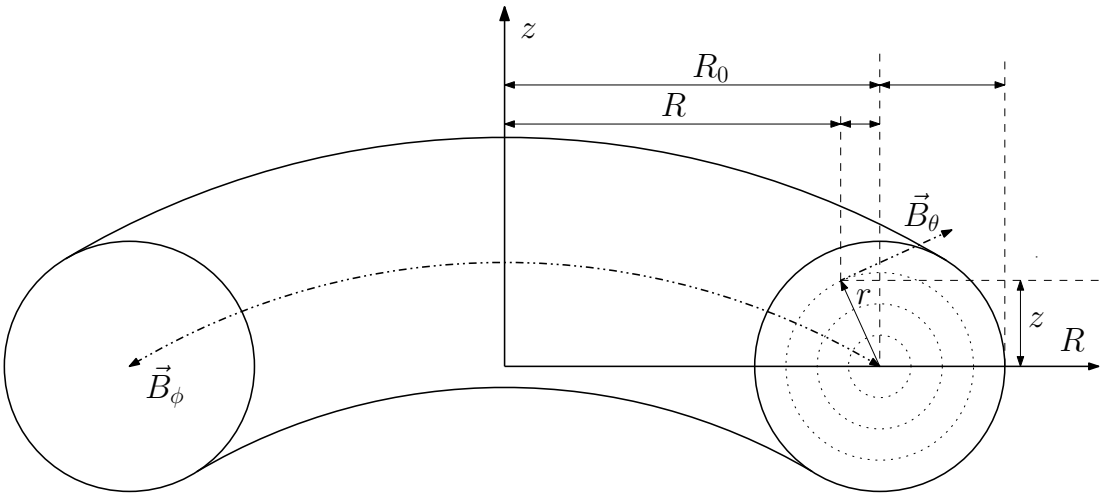

Figure 1.1: Used notation of the tokamak geometry.

1.3.1 Tokamak design

Charged particles in the homogeneous magnetic field do Larmor gyration and can move only parallel to the magnetic field; particles are frozen in the magnetic field.

A geometry and used notation of the tokamak is shown in Fig. 1.1. The tokamak uses a toroidal geometry with the toroidal field (Fig. 1.2) and thus there is the radially inhomogeneous magnetic field. As a consequence of the

Ampère's law is magnetic field proportional to $1/R$, where R is a distance from the torus axis. The magnetic field gradient points in a direction from the torus axis and thus, grad B drift vertically separates positive and negative charges and leads to formation of the electric field which causes $\vec{E} \times \vec{B}$ drift. These drifts lead to the plasma decay if no additional field is applied.

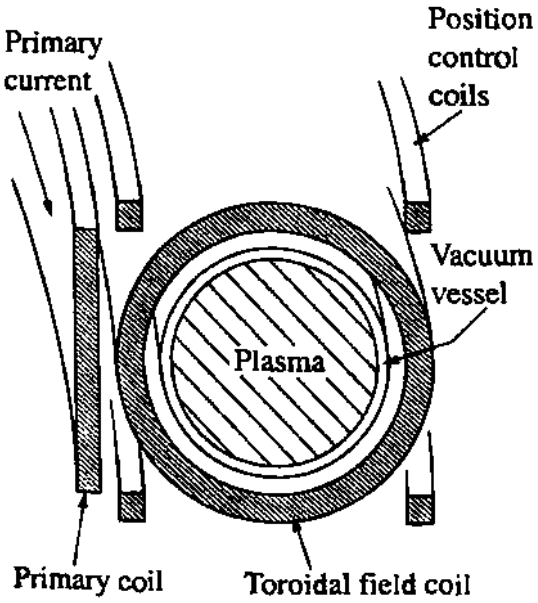

Figure 1.2: Arrangement of coils in a tokamak. The figure is taken from Wesson et al. [2004].

Drifts are removed if the plasma particles have a helical trajectory. Particles above the plasma center move up and in the direction from the plasma center. The particles below the plasma center move also up but closer to core. If the poloidal rotation is enough effective, the grad B drift disappears and the plasma stays quasineutral. The helical trajectory on tokamaks is obtained by a formation of the plasma current and, as a consequence, by the formation of a poloidal magnetic field. As the charged particles are frozen in the magnetic field, they perform the helical trajectory. The plasma current is generated using a transformer due to electromagnetic induction.

In addition, the plasma is affected by a curvature drift and the plasma expansion due to a different plasma pressures on inboard and outboard sides. These effects expand the plasma in the radial direction. This effect can be removed by applying the vertical magnetic field.

A circular shaped plasma is more susceptible to MHD activity (Chen [1984]) localized on rational magnetic surfaces (see Sec. 1.3.2). This activity can be suppressed by plasma elongation thus, the tokamak vessels have D-profiled coss-section and divertor magnetic geometry is used.

1.3.2 Safety factor, q

The safety factor, q, plays an important role in physics of confinement. In general, higher values of q lead to better stability. Each magnetic line is connected with its value of q. The magnetic lines with the same value of q determine single flux surface.

The magnetic field line follows due to poloidal field a helical path as it going round the torus. The magnetic field line returns to the same value of poloidal angle after the toroidal angle $\Delta\phi$. The q-value of this field line is defined as

$$q = \frac{2\pi}{\Delta\phi}. \tag{1.12}$$

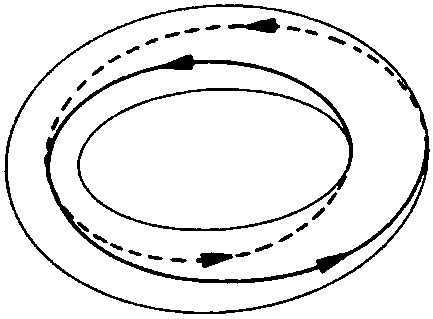

Figure 1.3: Field line on $q = 2$ magnetic surface.

Thus, if the magnetic line doing one poloidal turn during one toroidal turn has $q = 1$. If the magnetic line moves slowly in the poloidal angle it has a higher value of q (see Fig. 1.3). Magnetic surfaces with rational value of q play an important role for stability (e.g., magnetic reconnection occurs only on rational surfaces (Wesson et al. [2004])). If $q = m/n$, where $m \leq n$ are integers, the magnetic field line joints up on itself after m toroidal and n poloidal rotations round the torus. Thus, for small values of m and n there is a small *connection length*.

Single magnetic field line can be describe by equation

$$\frac{R\,\mathrm{d}\phi}{B_\phi} = \frac{\mathrm{d}s}{B_\theta}, \tag{1.13}$$

where $\mathrm{d}s$ is the distance in the poloidal direction, while moving through a toroidal angle $\mathrm{d}\phi$, B_ϕ, B_θ are toroidal and poloidal magnetic fields, R is a major radius of the field line on the toroidal angle ϕ. From (1.12) and (1.13), the value of q is:

$$q = \frac{1}{2\pi}\oint \frac{1}{R}\frac{B_\phi}{B_\theta}\,\mathrm{d}s, \tag{1.14}$$

where the integration path is over single circuit.

The value of q is the same for all magnetic lines on a magnetic surface. Thus q is a function of flux function, $q = q(\psi)$.

For a large aspect-ratio (Eq. (1.3)) with a circular cross-section, equation (1.14) can be approximated as

$$q = \frac{r}{R_0}\frac{B_\phi}{B_\theta}, \tag{1.15}$$

where r is a minor radius of the flux surface and B_ϕ is essentially constant toroidal magnetic field on the tokamak major radius R_0.

A typical radial profile of q has its minimum at or near to the magnetic axis and increases outward. In the case of circular plasma, the magnetic profile is approximated by

$$q(r) = \frac{2\pi r^2 B_\phi}{\mu_0 I(r) R_0}, \tag{1.16}$$

and the total current $I(r)$ is defined as

$$I(r) = 2\pi\int_0^r j(r')\,\mathrm{d}r',$$

where $j(r)$ is a current density on the magnetic surface with radius r.

Edge values of q are

$$q(r\to 0) \equiv q_0 = \frac{2B_\phi}{\mu_0 j_0 R_0}, \tag{1.17}$$

$$q(a) \equiv q_a = \frac{2\pi a^2 B_\phi}{\mu_0 I R}, \tag{1.18}$$

where $j_0 = \lim_{r\to 0} j(r)$ and I is the total current through the plasma.

The q-profile of the plasma can be obtained by numerical computation and usually involves solving Grad-Shafranov equation. In the divertor geometry, q_a goes to infinity (Wesson et al. [2004]) in the edge region. Thus, a q_{95} is used and is defined as safety factor on 95 % of the total magnetic flux.

In the case of a large aspect-ratio circular plasma, the current density profile can be expressed in approximation as[1]

$$j = j_0(1 - r^2/a^2)^\nu, \tag{1.19}$$

then the ratio of q gives

$$\frac{q_a}{q_0} = \nu + 1. \tag{1.20}$$

1.3.3 Toroidal effects

Mirror equation

When the charged particle moves to the magnetic field with more dense magnetic lines, it is affected by force $-\mu\nabla B$. If the gradient of the magnetic field is large enough, the particle can stop and return. Configuration where the particle is trapped in space by ∇B forces is called *magnetic mirror*.

Mirror equation can be obtained by considering the energy conversion law and adiabatic invariant μ (Kulhánek [2011])

$$\frac{\sin^2\alpha}{B} = \frac{\sin^2\alpha_0}{B_0}; \qquad B_C = \frac{B_0}{\sin^2\alpha_0}, \tag{1.21}$$

where α is the angle between magnetic lines and particle's velocity and B_0, α_0 are the initial magnetic field and angle, respectively. The particle velocity is with angle α connected by relations

$$v_\parallel = v \cdot \cos\alpha, \tag{1.22}$$

$$v_\perp = v \cdot \sin\alpha, \tag{1.23}$$

where $v_\parallel$ is component of velocity parallel to magnetic field line and $v_\perp$ component perpendicular to field line. It is easy to see that if the particle moved to the critical field B_C its $v_\parallel$ is equal to zero. Thus, at least B_C should be generated to form the magnetic mirror, otherwise the particle wound fly through the area of a more dense field.

[1] see Sec. 4.3

Banana orbits

In the tokamak geometry, the toroidal field behaves like $B_\phi \propto 1/R$. Thus, the stronger field is on the inboard side than on the outboard side. If the particle moves along the magnetic surface from the outboard side to the inboard area it can easily happen that the particle gets into the critical field B_C and it bounces it back. The particle is trapped in the outboard side. According to ∇B and curvature drifts, the particle does so call *banana orbit*. The study of the banana particles and their effects are part of *neoclassical theory*.

The condition for bounce the of particle can be formulated as (Kulhánek [2011], Dudson [2011])

$$\sin^2 \alpha_0 > \frac{R-r}{R+r}, \quad \text{or} \quad \left(\frac{v_{\|0}}{v_{\perp 0}}\right)^2 \leq 2\epsilon, \tag{1.24}$$

where ε is tokamak aspect-ratio (Eq. (1.3)), $v_{\|0}$ and $v_{\perp 0}$ are initiate velocity parallel and perpendicular to magnetic field lines, and α_0 is an initial angle between the magnetic line and the plane of Larmor rotation.

Bootstrap current

The plasma density n is decreasing from the plasma center to its edge. Two different banana orbits perambulate throw some points on the radial axis. Particles on orbits move against each other. The plasmas of these banana orbits have two different densities. This leads to formation of toroidal *bootstrap current* driven by the radial gradient of the plasma density (Wesson et al. [2004])

$$j_b \sim -\sqrt{\varepsilon}\frac{T}{B_\theta}\frac{\mathrm{d}n}{\mathrm{d}r}, \tag{1.25}$$

where T is a plasma temperature.

1.4 Compass tokamak

The Compass (**COMP**act **ASS**embly) tokamak is a main experimental device of the Tokamak Department of Institute of Plasma Physics (IPP) AS CR[2]. The Compass tokamak has been designed and build in British Culham Science Centre

[2]The Academy of Science of the Czech Republic.

as a flexible research facility dedicated mostly to plasma physic studies in circular and D-shaped plasmas[3].

The Compass tokamak is together with ASDEX-Upgrade in Germany and JET in Britain from the group of tokamaks with an ITER-relevant geometry and is used as scale experiment for ITER. Compass is the smallest from this group and thus it is very flexible to new experiments and testing of new technologies. Typical Compass parameters are presented in Tab. 1.1.

The Compass tokamak is well equipped with diagnostics[4] focused on edge plasma physics. Here, investigations focused on study of transition between low (L-mode) and high (H-mode) confinement modes. With the H-mode, edge localized mods (ELMs) are connected. Other studies deal with turbulence in the tokamak plasmas and particle transport.

Parameters	**Current values**	**Expected max. values**
Major radius R	0.56 m	0.56 m
Minor radius a	$0.18 - 0.23$ m	$0.18 - 0.23$ m
Plasma current I_p (max)	200 kA	350 kA
Magnetic field B_T (max)	1.3 T	2.1 T
Vacuum pressure	2×10^{-6} Pa	2×10^{-6} Pa
Elongation	1.7	1.8
Plasma shape	D, SND, elliptical, circular	D, SND, elliptical, circular
Pulse length	~ 0.3 s	~ 1 s
Beam heating P NBI 40 keV	1×0.3 MW	2×0.3 MW

Table 1.1: Parameters of compass tokamak. http://www.ipp.cas.cz/Tokamak/euratom/index.php/en/compass-parameters.

[3] http://www.ipp.cas.cz/Tokamak/euratom/index.php/en/compass-general-information

[4] Detail description of the Compass diagnostics is given in Chap. 2.

2. Compass diagnostics

The compass tokamak is well equipped with diagnostics focused on H-mode and pedestal investigations (Weinzettl et al. [2011]). The Compass diagnostics include magnetic, spectroscopy, microwave, probe and beam diagnostics. Overview of diagnostics is given in Fig. 2.1.

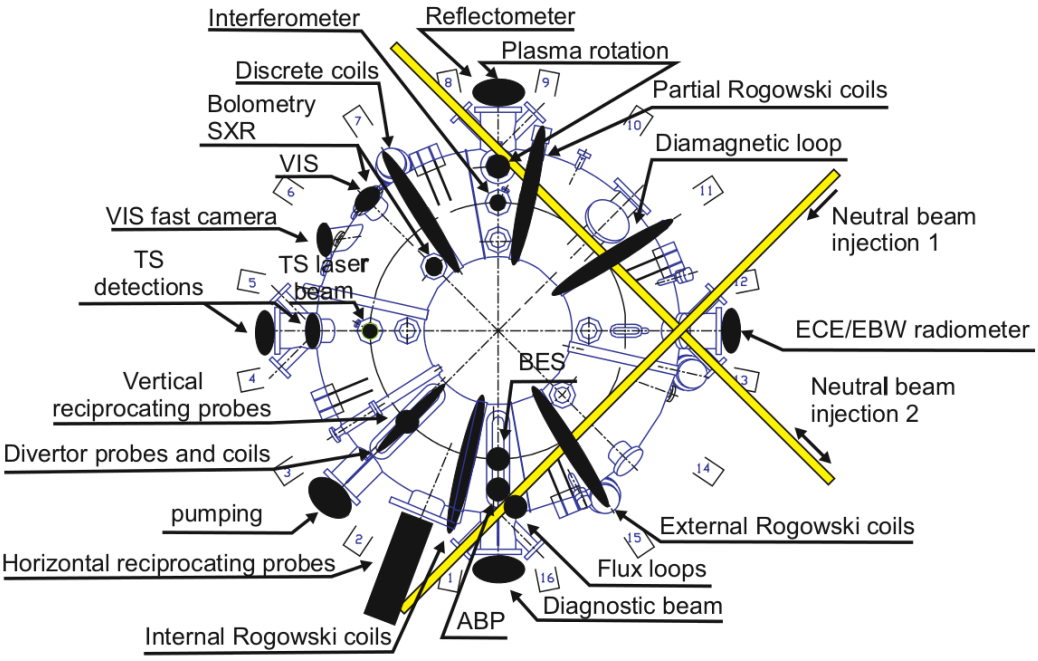

Figure 2.1: Overview of the Compass diagnostics (top view). The figure is taken from (Weinzettl et al. [2011]).

2.1 Magnetic diagnostics

The most of magnetic measurements are based on Faraday's law (4.5) and/or Ampère's law (4.4). The usual magnetic coil and inductive loop diagnostics are shown in Fig. 2.2 and partial coils in Fig. 2.3.

Instead of local magnetic field, the magnetic flux is measured. The magnetic flux through a some closed area S (for example area of a tokamak chamber) is defined as

$$\Phi = \int_S \vec{B}\,\mathrm{d}\vec{S}. \tag{2.1}$$

Normal (integral) variation of Faraday's law can be obtained by integrating Eq. (4.5) through the area S and using Stokes theorem:

$$\int_S \frac{\partial \vec{B}}{\partial t}\,\mathrm{d}\vec{S} = -\int_S \mathrm{rot}\,\vec{E}\,\mathrm{d}\vec{S}, \tag{2.2}$$

$$\frac{\partial}{\partial t}\int_S \vec{B}\,\mathrm{d}\vec{S} = -\oint_{\partial S} \vec{E}\,\mathrm{d}\vec{\ell}, \tag{2.3}$$

$$V = \frac{\partial \Phi}{\partial t}, \tag{2.4}$$

where V is measured voltage (Hutchinson [2002]).

From the previous paragraph it follows that a typical loop diagnostic (see examples in Fig. 2.2) measures time derivation of the magnetic flux through it. However, one is typically interested in Ψ rather than in $\dot{\Psi}$, thus, an integration element is generally used to obtain Ψ.

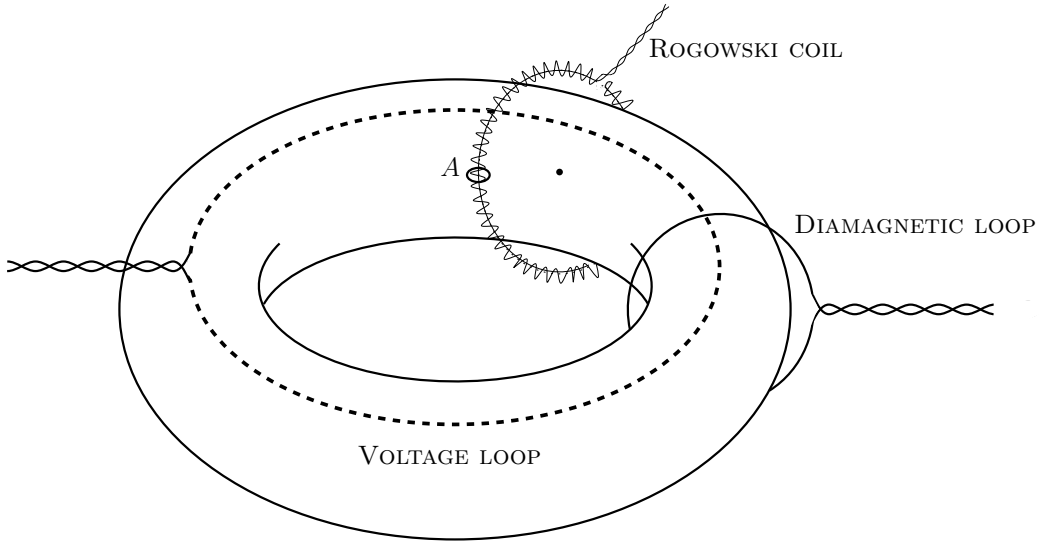

Figure 2.2: Overview of some inductive loops diagnostics.

2.1.1 Rogowski coils

Rogowski coil is the solenoidal coil which is stretched around the vessel, as it is illustrated in Fig. 2.2. The electric current in the tokamak vessel can be determined by integrating Ampère law (4.4) through the vessel area

$$\mu_0 I = -\int_S \mathrm{rot}\,\vec{B}\,\mathrm{d}\vec{S}$$

and using the Stokes' theorem is

$$\mu_0 I = -\oint_{\partial S} \vec{B}\,\mathrm{d}\vec{\ell} \tag{2.5}$$

obtained.

Magnetic flux through the Rogowski coil (see Fig. 2.2) is according to its geometry given as

$$\Phi = n \int \int_A \vec{B}\,\mathrm{d}A\,\mathrm{d}\vec{\ell}, \tag{2.6}$$

where n is the number of loops per unit length. If the magnetic field doesn't change within one loop, Eq. (2.6) can be rewritten as

$$\int \vec{B}\,\mathrm{d}\vec{\ell} = \frac{\Phi}{nA}. \tag{2.7}$$

Comparing Eq. (2.7) with Eq. (2.5) leads to

$$I_\phi = -\frac{\Phi}{nA\mu_0}. \tag{2.8}$$

Thus, the Rogowski coil wounded around the vessel is able to measure a total electric current through the plasma.

The Compass tokamak is equipped by 6 commercial Rogowski coils MFC 150 for measurements of the current in the poloidal and toroidal field coil circuits, then by one internal (external) Rogowski coil wound inside (around) the vacuum vessel for measurements of the plasma current I_p (sum of I_p and vessel current).

2.1.2 Voltage loop

As it has been introduce in Sec. 1.3.1 and illustrated in Fig. 1.2, the plasma current surrounded by the vessel is induced be transformer core. The toroidal loop voltage can be measured by so call *voltage loop* or *flux loop* which is a wire encircling the torus as it is illustrated in Fig. 2.2.

If the plasma current is stable in time a plasma resistivity and a ohmic power can be measured using the Rogowski coil and voltage loop. A plasma resistivity R can be simply determined as a ratio of the toroidal voltage V_ϕ and the poloidal plasma current I_ϕ.

$$R = \frac{V_\phi}{I_\phi} \tag{2.9}$$

and the Ohmic power P as

$$P = V_\phi I_\phi. \tag{2.10}$$

If the plasma current varies in time, a situation isn't so simple, and Poynting's theorem should be used. This case is described in Hutchinson [2002] in details.

The Compass tokamak is equipped with 8 flux loops with integration for measurements of the poloidal flux function and 8 flux loops without integration for measurements of the loop voltage U_{loop}.

2.1.3 Diamagnetic loop

Diamagnetic loop is a wire wounded around the torus and designated for measurement of the toroidal magnetic flux and thus for determination the average value of $\langle B_\phi \rangle = \Phi / S$, where S is a surface of the vessel.

The diamagnetic loop can be also used to determine the energy stored in the plasma (Hutchinson [2002]). The stored energy is computed from magnetic fluctuations due to a generated magnetic field. Two diamagnetic loops on the Compass tokamak are designed for such measurements.

2.1.4 Mirnov coils and internal partial Rogowski coils

The magnetic field in a poloidal cross-section is not generally homogeneous and even non-radially symmetric. For a measurement of local poloidal magnetic instabilities, a set of poloidally deployed coils can be used. Example of these coils are Mirnov and IPR coils, both used on the Compass tokamak (see Fig. 2.3).

As the Rogowski coil is wounded around the vessel, internal partial Rogowski (IPR) coil is poloidally wounded only around an approximately 4 cm inside the vessel on the Compass tokamak. Such wound coil is capable to measure a local poloidal magnetic field.

Mirnov coils have been developed for measurements of magnetic field changes in space. Mirnov coil compounds of three very small coils, each oriented orthogonally to others. On the tokamak, there are placed to measure toroidally, poloidal and radial components of the magnetic field separately. On the tokamak, at different toroidal places, three rings are placed. Each ring contains 24 poloidally

deployed Mirnov coils. However, only one ring which measures a poloidal component of the magnetic field is currently in use.

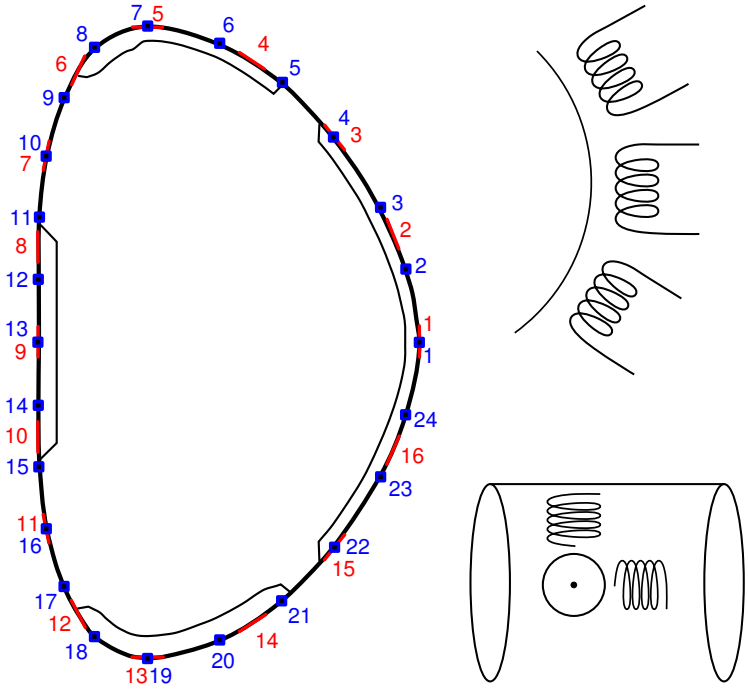

(a) (b)

Figure 2.3: Illustration of partial coils. (a) The poloidal distribution of the Mirnov coil on Compass is shown in blue and the poloidal distribution of IPR coils is shown in red. (b) The illustration of IPR coils (up) and Mirnov coils (down).

#	R [m]	z [m]	Angle [°]	Calib.	Channel
1	0.7885	0	-90	0,0842	17
2	0.75629997	0.13169999	-66.349998	0.0878	18
3	0.685	0.24950001	-51.0077	-0.0878	19
4	0.58490002	0.3425	-31.991501	-0.0849	20
5	0.45739999	0.3829	0	-0.0879	21
6	0.37259999	0.33129999	61.985291	-0.0864	22
7	0.33340001	0.22660001	78.330528	-0.0884	23
8	0.324	0.1155	90	-0.0848	24
9	0.324	0	90	0.0876	25
10	0.324	-0.1155	90	0.0878	26
11	0.33340001	-0.22660001	101.66947	0.0272	27
12	0.37259999	-0.33129999	118.01471	0.0275	28
13	0.45739999	-0.3829	180	0.0877	29
14	0.58490002	-0.3425	-148.00085	0.0866	30
15	0.685	-0.24950001	-128.9922	0.0860	31
16	0.75629997	-0.13169999	-113.65	0.0808	32

Table 2.1: Table of IPR coils, their position, relative calibration and source channel.

#	R [m]	z [m]	Angle [°]	Calib.	Channel
01	0.7892	0.00	90	0.1151	23
02	0.7729	0.089	107.856223257315	0.1159	24
03	0.7411	0.1632	117.233949353729	XXX	3
04	0.6845	0.25	128.153793029543	0.1206	4
05	0.6213	0.316	138.36646066343	XXX	7
06	0.5447	0.3637	157.382482662362	0.1153	8
07	0.4575	0.3845	178.840201258382	0.1343	1
08	0.3934	0.3594	220.650787099881	0.1135	2
09	0.3553	0.2981	247.965797526476	0.1146	5
10	0.3336	0.2265	258.701999175019	XXX	6
11	0.3249	0.1522	88.278926143816	0.1188	9
12	0.3245	0.0762	90	0.1166	10
13	0.3245	0	90	0.118	11
14	0.3244	-0.0762	90.5787255656079	0.1168	12
15	0.3252	-0.1522	91.1597987416179	0.1146	15
16	0.3335	-0.2265	101.888655613873	0.1171	16
17	0.3553	-0.2981	112.034202473524	0.1149	19
18	0.3933	-0.3594	139.349212900118	0.1137	20
19	0.4575	-0.3845	181.159798741618	0.1229	13
20	0.5444	-0.3631	202.508313315783	0.1161	14
21	0.621	-0.315	222.145095203157	XXX	17
22	0.6846	-0.25	232.298114854022	0.1186	18
23	0.7411	-0.1633	63.0649501281735	0.1181	21
24	0.7728	-0.089	72.1644789063985	0.1197	22

Table 2.2: Table of Mirnov coils, their position, relative calibration and source channel.

2.2 Soft X-ray

Accelerated charged particle emits electromagnetic radiation, so call *bremsstrahlung*. Bremsstrahlung spectrum in the plasma originates mainly from electrons in Coulomb field of ions. The bremsstrahlung is temperature and density dependent and lies mainly in the soft X-Ray[1] (SXR) range. The bremsstrahlung is also the main source of SXR radiation on the Compass tokamak (Imríšek et al. [2013]). Considering only non-relativist physics, the radiation power is proportional to

$$P_{\text{brem}} \propto Z_{\text{eff}} n_e^2 \sqrt{T_e}, \tag{2.11}$$

where n_e is the electron density, T_e the electron temperature, $Z_{\text{eff}} = \sum_i n_i Z_i^2 / n_e$ is effective charge, n_i is the ion density and Z_i is the ion charge.

The SXR signal is measured by a pinhole camera with array of photodiodes. This configuration enables chord-integrated measurements of the SXR radiation and together with another field of the SXR detector they provide data source for the SXR tomography (Mlynar et al. [2012]).

The Compass tokamak (Imríšek et al. [2013]) is equipped with two LD 35-5T SXR detectors with 35 channels each. Low energy photons[2] are shielded by 10 μm Be foil. Transmittance of diodes also given by a thickness of active layer of $d_{\text{active}} = 200\,\mu\text{m}$, passive layer of $d_{Si_3N_4} = 0.55\,\mu\text{m}$ and diode dead layer with the thickness of $d_{\text{dead}} = 0.6\,\mu\text{m}$. Spectral sensitivity of diodes is given by formula

$$f(E) = \exp(-\mu_{Be} d_{Be} - \mu_{Si} d_{\text{dead}} - \mu_{Si_3N_4})(1 - \exp(-\mu_{Si} d_{\text{active}})), \tag{2.12}$$

where μ_{Be}, μ_{Si} and $\mu_{Si_3N_4}$ are absorption coefficients. The plot of spectral transitivity is shown in Fig. 2.4.

[1] Energies in the range of 5–10 keV.

[2] Photons with the energy below 0.5 keV.

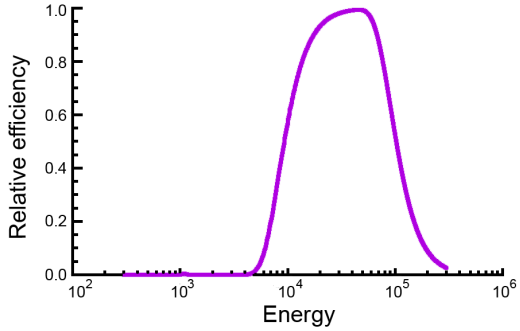

Figure 2.4: Relative efficiency of the SXR detection using thin beryllium foil. The figure is taken from http://www.ipp.cas.cz/Tokamak/euratom/index.php/en/compass-diagnostics/spectroscopic/soft-x-rays.

2.3 Other relevant diagnostics on Compass tokamak

2.3.1 Spectroscopic diagnostics

Aside two SXR cameras, tomography reconstruction could be done by six AXUV bolometers (7 eV – 6 keV). AXUV detectors are separated to four poloidally separated ports with 20-channel detector arrays each. Two ports on LFS are equipped with a pair of AXUV detectors. The range of spectroscopic diagnostics complement photo-multipliers with interference filters for H, C_{III} and Z_{eff} lines and spectrometers for near ultra-violet (248 – 472 nm), visible light (457 – 663 nm) and H_α (630 – 680 nm) regions. Data of SXR, bolometers and visible light diagnostics are measured with the frequency of 2 MHz.

The Compass tokamak is equipped with the Thomson scattering system to measure density and temperature radial profiles of the plasma. The Thomson scattering is consisted of two Nd:YAG lasers (1064 nm, 1.5 J, 30 Hz) with a pulse separation in the range of 1 μs – 17.7 ms.

The plasma rotation can be determined by measuring of the Doppler shift C_{III} (C^{2+}) impurity spectral line using high-dispersion spectrometer.

Spectroscopic diagnostics complement two visible cameras EDICAM, one is poisoned tangentially and second vertically on HFS, and one slow IR camera.

2.3.2 Microwave diagnostics

Plasma density is measured by two interferometers working on 131 GHz and 133 GHz. The signal is registered on one vertical chord going through the tokamak geometrical center. The signals from the detectors are calibrated on the circular plasma with a magnetic center identical to the geometrical and with diameter of 40 cm. However, the plasma is usually shifted[3] and shaped. To obtain right values of the density, diagnostic data should be corrected using data from the EFIT reconstruction.

The Compass tokamak microwave diagnostics enclose radiometer and reflectometer. The existing radiometer will be used for electron cyclotron emission (ECE) measurements of the island width.

2.3.3 Other diagnostics

Edge localized plasma potential, electron density, and temperature could be measured with Compass probe diagnostics as well as parallel flow and flow towards the wall. Compass diagnostics system encloses the beam emission spectroscopy (BES), atomic beam probe diagnostics (ABP) and neutral particle analyser (NPA). ABP, BES and NPA diagnostics are currently under development.

[3] At least due to Shafranov shift.

3. Data processing

3.1 Discrete Fourier Transform (DFT)

Fourier series are using to decompose a function into sum of a orthogonal functions. If the trigonometric base on an interval τ

$$\{\mathrm{e}^{-2\pi i\frac{kx}{\tau}};\quad k\in\mathbb{Z}\}$$

is used, a function is decomposed into frequencies. Then the appropriate frequency coefficients H_n has a meaning of the weight of the frequency f_n.

The DFT is widely used technique even on non harmonic signal. If the processed signal isn't harmonic, the inner structure of signal is displayed in higher harmonic frequencies.

Discrete Fourier transform and inverse DFT are defined with respect to continuous Fourier series. Let f_s is the sampling frequency and $T_s = 1/f_s$ is the sampling interval of the signal then DFT is defined as (Press et al. [2007])

$$H_n = \sum_{k=0}^{N-1} h_k \mathrm{e}^{2\pi i\frac{kn}{N}};\quad f_n = \frac{n}{NT_s} \tag{3.1}$$

and inverse transform is defined as

$$h_k = \frac{1}{N}\sum_{n=0}^{N-1} H_n \mathrm{e}^{-2\pi ikn/N}. \tag{3.2}$$

The obtained value of DFT is complex. Absolute value of H_n corresponds to strength of the frequency f_n and argument of H_n corresponds to phase of the frequency.

Second power of the term H_n represents "power" of frequency f_n. The term H_n have to be divided by half of the signal length to obtain complex amplitude A_n of frequency f_n

$$A_n = \frac{2H_n}{N}. \tag{3.3}$$

Let's define a total power of signal as a sum of squared amplitudes

$$W = \sum_{k=0}^{N-1} |h_k|^2. \tag{3.4}$$

The total power in frequency domain can be obtain by using *Parseval's theorem*

$$\sum_{k=0}^{N-1} |h_k|^2 = \frac{1}{N} \sum_{n=0}^{N-1} |H_n|^2. \tag{3.5}$$

Thus the power of a given frequency f_n, consistently with definition (3.4), can be calculated as $|H_n|^2$.

For signal with sampling interval T_s *Nyquist frequency* is defined as

$$f_{\mathrm{nq}} \equiv \frac{1}{2T_s}. \tag{3.6}$$

Nyquist specifies the highest recognisable frequency in the signal. This fact is represented in *sampling theorem* (Press et al. [2007]): "If a continuous function $h(t)$, sampled at an interval T_s, happens to be *bandwidth limited* to frequencies smaller in magnitude then f_{nq}, i.e., if $H(f) = 0$ for all $|f| \geq f_{\mathrm{nq}}$, then the function $h(t)$ is completely determined by its samples h_n."

However, if the measured signal is not bandwidth limited, the phenomenon called *aliasing* appears in the frequency domain. This means that larger frequencies are mirrored to a lower bend. This phenomenon is well illustrated in Fig. 3.1.

The Nyquist frequency of the most of Compass diagnostics is above 1 MHz and observed signal is usually tens of kHz. Thus aliasing does not spoil measured signal.

3.1.1 Fast Fourier Transform

Discrete Fourier transform computed from definition (3.1) has quadratic time complexity $\mathcal{O}(N^2)$. This complexity is enormous for large data set. Fortunately, there is a way how to computed DFT faster. This set of algorithms is called fast Fourier transform (FFT) and has logarithmic time complexity $\mathcal{O}(N \log N)$.

For the purposes of this work, implementation of MATLAB[1] and SciPy[2] have been used. Because the FFT time complexity is very optimistic it is also used in other processing techniques.

[1] http://www.mathworks.com/products/matlab/

[2] http://www.scipy.org/

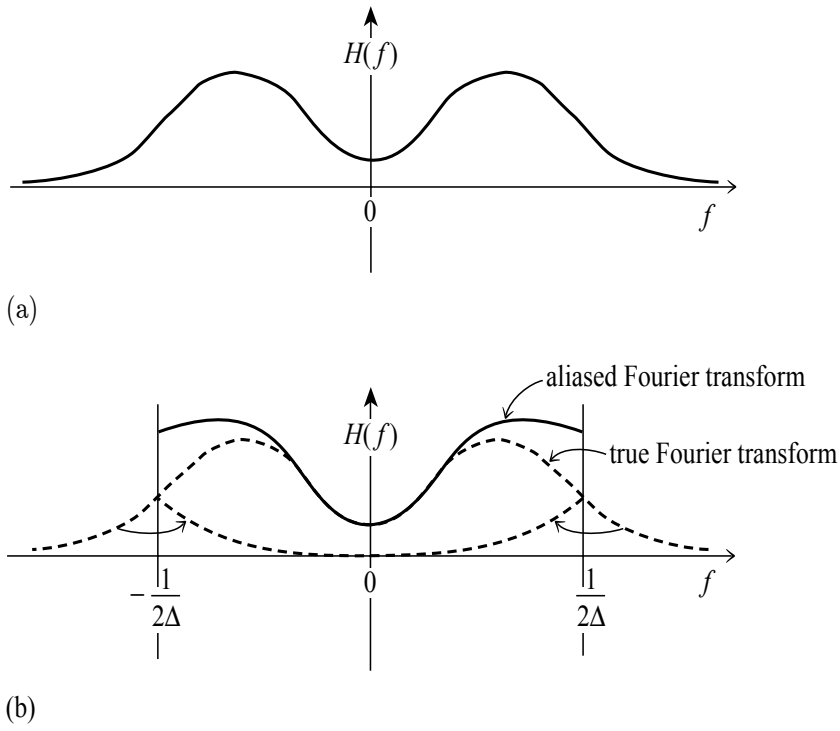

Figure 3.1: Illustration of aliasing. The figure is taken form Press et al. [2007].

3.1.2 Power spectrum

Final sampling frequency and discrete character leads to *spectral leakage* (Press et al. [2007]). This effect enlarges if the signal's frequency is in the range (f_n, f_{n+1}) for some natural n. This effect can be partially removed using s window function. Where the transformed window is multiplied by a window function. In the thesis, square, Barlett's (triangular) and Welch's window functions have been implemented.

The frequency spectra in the thesis are plotted as a square root of frequency power.

3.2 Cross-correlation function

The cross-correlation technique measure similarity of two signals shifted in time. It is defined as

$$\mathrm{Corr}(g,h)_t = \sum_{k=0}^{N-1} g_{t+k} h_k. \tag{3.7}$$

Result of cross-correlation is a function of the *lag* t. The lag lies in the range $\langle -N, N \rangle$.

The value of cross-correlation function defined as (3.7) isn't normalized and depend on lengths and magnitudes of the signals. Implementation of cross-correlation used in this thesis is normalized to standard deviation or to one, according to situation.

Algorithm can be speed up using FFT and *correlation theorem*

$$\widehat{\mathrm{Corr}(g,h)}(f_n) = G(f_n)H^*(f_n) \tag{3.8}$$

where $\widehat{\mathrm{Corr}(g,g)}(f)$ means Fourier transform of cross-correlation function and $H^*(f_n)$ represent complex conjugation of H. Correlation theorem gives a way to a faster algorithm. Cross-correlated signals are transformed by FFT, multiplied and inverse FFT (IFFT) is applied on the resulted vector. The result of this operation is equivalent to correlation defined by (3.7).

Cross-correlation technique applied on IPR coils signal is shown in Fig. 3.2 (a). The IPR coils are deployed around the poloidal angle of tokamak vessel. Coils detect poloidaly moving instability. Cross-correlation can visualised the instability movement.

The correlation theorem has one more advantage. The autocorrelation function[3] has a same spectrum as the original signal. Thus, if one signal is measured on two detectors then its cross-correlation function has the frequency spectrum of the original signal with a noise suppression. This technique have been also implemented, especially for magnetic and bolometric detectors.

[3]Cross-correlation of one signal.

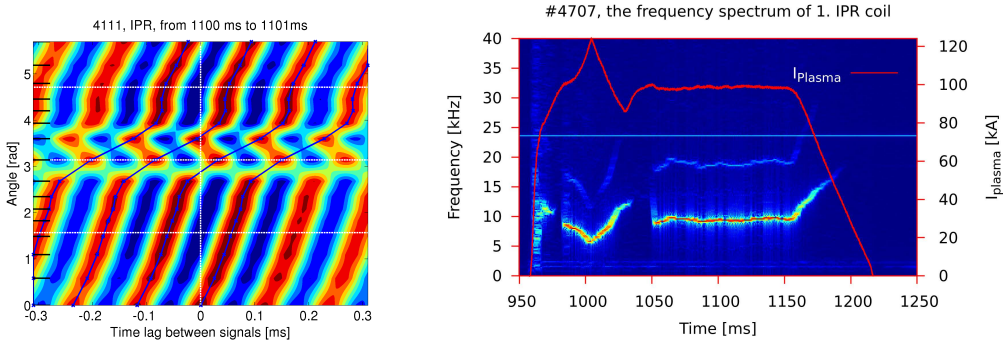

(a) (b)

Figure 3.2: Example of (a) cross-correlation and (b) DTFFT result. On the cross-correlation graph there are three rotating islands. The islands are rapidly slowing down on HFS (middle dashed line).

3.3 Discrete Time Fast Fourier Transform

Time development of signal frequencies (spectrogram) can be observed using Discrete Time Fast Fourier Transform (DTFFT) technique. The signal is separated into overlapping short time windows. FFT is applied on each window. The amplitude can be plotted in a 3–D graph as a function of the time and frequency (see Fig. 3.2 (a)).

If a spectral filter is applied on spectrogram, a filtered signal can be obtained. In the thesis, the signal is reconstructed as a mean of inverse transform magnitude. One single time of signal is used several times in spectrogram due to overlapping time windows. Thus, the signal in time domain has to be composed from more discrete times in frequency domain.

Example of the spectrogram is shown in Fig. 3.2 (b). First IPR coil detect MHD activity on approximately 12 kHz and its higher harmonics. The color scale of the figure is logarithmic.

3.4 Other used data processing technique

3.4.1 Tracking

It can be useful to detected traces of functions peaks in both examples in Fig. 3.2 . In the case of DTFFT tracking is advantageous to distinguish the an amplitude and a frequency time profile of concrete MHD activity. Tracking in Fig. 3.2 (a) can be used to indicate MHD activity. If the MHD activity is indicated, the tracking is able to determine mode number and, in combination with the EFIT, to measure the velocity of the instability.

3.4.2 Smoothing

The signal obtained from detector contains, beside the MHD activity within a specific range, a high frequency noise and a trend given by other phenomena in tokamak. The MHD activity can be highlighted using high-frequency and low-frequency filter (so-called band pass filter).

In the thesis, as a high frequency filter *Savitzky–Golay (S–G) smoothing algorithm* (Savitzky and Golay [1964]) has been implemented. This algorithm applied on time window much shorter then specific period of MHD activity have been used to reduce signal noise.

The low frequency filter has been implemented with usage of S–G filter. The original signal has been smoothed by S–G filter set on time window much longer then specific period of observed MHD activity. The resulted signal for other techniques has been obtained by subtracting smoothed from the original signal.

3.4.3 Signal envelope

Detection of a signal envelope is important to observe amplitude development. In the thesis, the envelope detection is implemented via the Hilbert transform. The Hilbert transform is convolution of the signal with the Cauchy kernel $1/\pi t$. An absolute value of a signal's Hilbert transform is envelope of the signal. An example of envelope detection is shown in Fig. 5.17 on page 63.

4. Magnetohydrodynamics

4.1 Formulation of magnetohydrodynamics

There are various method how to describe the tokamak plasma. Some of them are more complex and also more complicated. All physical information about plasma can be obtained only from the full kinetic model (Park et al. [1999]). Analytical solution of such model cannot be found in general. It has been shown that a significant part of plasma behavior can be explained with the single fluid model considering continuum equations from hydrodynamics and equations derived from Maxwell equations from electrodynamics. This access is called *magnetohydrodynamics* (MHD).

The MHD description of plasma require following assumptions

1. quasineutrality ($n_e \approx n_i$),

2. continuum – characteristic size of system is much larger than a mean free paths of particles and their Larmor radius and time-scales of observarions are much larger than collision times and cyclotron times;

3. single fluid – plasma is locally close to thermodynamic equilibrium.

In addition to these assumptions, plasma is usually considered to be non-resistive. This case is called *ideal MHD*. If the finite resistivity is considered *resistive MHD* is used.

The list of ideal MHD equations follows (Wesson et al. [2004])

$$\frac{\mathrm{d}\rho}{\mathrm{d}t} = -\rho \,\mathrm{div}\, \vec{v} \qquad \text{(mass conservation)}, \tag{4.1}$$

$$\rho \frac{\mathrm{d}\vec{v}}{\mathrm{d}t} = \vec{j} \times \vec{B} - \,\mathrm{grad}\, p \qquad \text{(eqn. of motion)}, \tag{4.2}$$

$$\frac{\mathrm{d}p}{\mathrm{d}t} = -\gamma p \,\mathrm{div}\, \vec{v} \qquad \text{(adiabatic equation)}, \tag{4.3}$$

$$\mu_0 \vec{j} = \,\mathrm{rot}\, \vec{B} \qquad \text{(Ampère's law)}, \tag{4.4}$$

$$\frac{\partial \vec{B}}{\partial t} = -\,\mathrm{rot}\, \vec{E}, \qquad \text{(Faraday's law)} \tag{4.5}$$

$$0 = \vec{E} + \vec{v} \times \vec{B}, \tag{4.6}$$

where ρ is mass density, $\vec{v}$ the fluid velocity, $p = nk_BT$ the plasma pressure, $\vec{j}$ current density, γ adiabatic index, μ_0 permeability of vacuum, and $\mathrm{d}/\mathrm{d}t$ is so called substantial derivative (Kulhánek [2011])

$$\frac{\mathrm{d}\vec{A}}{\mathrm{d}t} = \frac{\partial \vec{A}}{\partial t} + (\vec{v}\cdot\nabla)\vec{A}, \quad \text{or} \tag{4.7}$$

$$\frac{\mathrm{d}\phi}{\mathrm{d}t} = \frac{\partial \phi}{\partial t} + (\vec{v}\cdot\nabla)\phi. \tag{4.8}$$

The case of resistive MHD can be obtained by a simple modification of previous equations. The third mentioned equation of electromagnetic field (4.6) could be substituted by Ohm's law

$$\vec{E} + \vec{v}\times B = \eta\vec{j} \tag{4.9}$$

and the adiabatic equation (4.3) by

$$\frac{\mathrm{d}}{\mathrm{d}t}\left(\frac{p}{\gamma-1}\right) = -\frac{\gamma}{\gamma-1}p\,\mathrm{div}\,\vec{v} + \eta j^2, \tag{4.10}$$

where η is the resistivity of the plasma.

Sometimes, the fluid is taken as incompressible; in this case $\mathrm{d}\rho/\mathrm{d}t = 0$ and $\mathrm{div}\,\vec{v} = 0$.

4.1.1 Equation of the magnetic field

Time development of the magnetic field can be obtained from equations (4.4), (4.5) and (4.9)

$$\frac{\partial \vec{B}}{\partial t} = \frac{\eta}{\mu_0}\Delta\vec{B} + \mathrm{rot}\,\vec{v}\times\vec{B}. \tag{4.11}$$

First term in Eq. (4.11) is like a classical diffusion – slow penetration of magnetic field to the plasma. The diffusion term is equal to zero in the case of ideal MHD[1].

Second term represents frozen magnetic fluid in the flowing plasma. Equation

$$\frac{\partial \vec{B}}{\partial t} = \mathrm{rot}\,\vec{v}\times\vec{B} \tag{4.12}$$

can be adjusted to the form

$$\frac{\mathrm{d}\vec{B}}{\mathrm{d}t} = (\vec{b}\cdot\nabla)\vec{v}, \tag{4.13}$$

[1] Eq. (4.6)

which is identical to the equation of stream line (Kulhánek [2011])

$$\frac{\mathrm{d}\delta\vec{l}}{\mathrm{d}t} = (\delta\vec{l}\cdot\nabla)\vec{v}. \tag{4.14}$$

As a consequence, magnetic field follows streamlines and is 'frozen in' the plasma.

Dominant term can be determined be the magnetic Reynolds number

$$\#_{Re,M} = \frac{\text{'frozen in' term}}{\text{diffusion term}} = \frac{\mu v L}{\eta}, \tag{4.15}$$

where L is specific size of system. This number indicate whether the ideal MHD or resistive MHD should be used.

4.2 Plasma equilibrium

Derivative of the plasma velocity is equal to zero in the equilibrium. Thus, equilibrium equation results from Eq. (4.2)

$$\nabla p = \vec{j}\times\vec{B}. \tag{4.16}$$

If the scalar product of current density $\vec{j}$ and magnetic field $\vec{B}$ on Eq. (4.16) is used, it can be written

$$\vec{j}\cdot\nabla p = 0; \quad \text{or} \quad \vec{B}\cdot\nabla p = 0 \tag{4.17}$$

Therefore, the electric current follows surface of the constant pressure as well as the magnetic lines. Magnetic lines and lines of the electric current aren't parallel in the general case, but they lie on the surfaces of the constant pressure.

4.3 Plasma flow

A solution which describe flow of fluid between tho parallel boards in the presence of pressure gradient is known in the classical fluid mechanic. This *laminar* solution behave in accord with the Poiseuille's law. Fluid has parabolic profile and zero velocity at the edges.

A solution similar to Poiseuille's can be found in the plasma. Let's consider incompressible viscose electromagnetic fluid. Then, the system of equations can

be written as (Kulhánek [2011])

$$\begin{aligned} \operatorname{div} \vec{u} &= 0, \\ \rho\frac{\partial \vec{v}}{\partial t} + \rho(\vec{v}\cdot\nabla)\vec{v} &= -\nabla p + \zeta\Delta\vec{v} + \left[\frac{\operatorname{rot}\vec{B}}{\mu_0}\times\vec{B}\right], \\ \frac{\partial \vec{B}}{\partial t} &= \frac{\eta}{\mu_0}\Delta\vec{B} + \operatorname{rot}[\vec{v}\times\vec{B}], \end{aligned}$$

where ζ is a *dynamic viscosity*. The solution will be considered in the form

$$\vec{v} = [v(y), 0, 0]; \quad \vec{B} = [B(y), B_0, 0]; \quad p = p(x, y). \tag{4.18}$$

The solution can be found as

$$v(y) = v_0\frac{\cosh\left(\frac{a}{D}\right) - \cosh\left(\frac{y}{D}\right)}{\cosh\left(\frac{a}{D}\right) - 1}, \tag{4.19}$$

$$B(y) = v_0\mu_0\sqrt{\frac{\zeta}{\eta}}\frac{\sinh\left(\frac{y}{D}\right) - \frac{y}{a}\sinh\left(\frac{a}{D}\right)}{\cosh\left(\frac{a}{D}\right) - 1}, \tag{4.20}$$

$$D \equiv \sqrt{\frac{\eta\zeta}{B_0^2}}, \tag{4.21}$$

where D is a characteristic width of the edge area. Geometry of problem is shown in Fig. 4.1 (a).

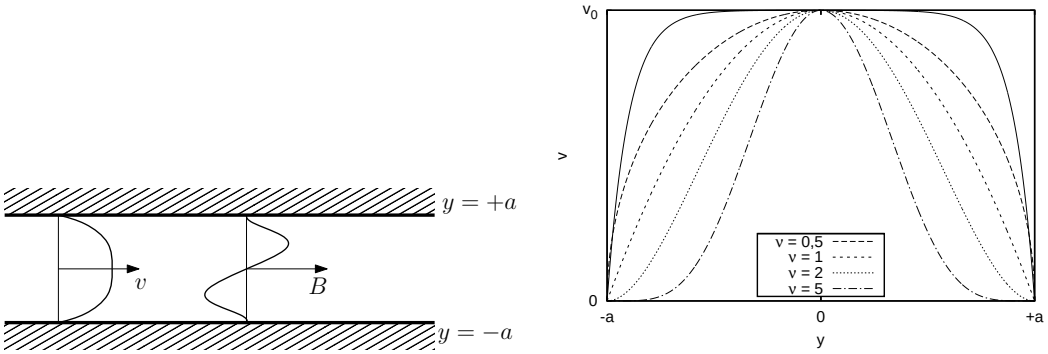

(a) (b)

Figure 4.1: (a) Geometry of stream tube with the velocity and magnetic field profiles. (b) Ideal current profiles for various ν in Eq. (4.24). Profile from Eq. (4.23) is plotted with the solid line.

Interesting result can be obtained in the case of week ($a/D \ll 1$) and strong fields ($a/D \gg 1$).

In the limit of a week field, the Poiseuille's parabolic profile is obtained

$$v \approx v_0 \left[1 - \left(\frac{y}{a}\right)^2\right]. \tag{4.22}$$

In the case of a strong field, the profile can be an approximated by exponential function

$$v \approx v_0 \left[1 - \exp\left(\frac{|y| - a}{D}\right)\right] \tag{4.23}$$

The solution (4.19) is for a simple manipulation quite complicated; thus the profile in form (Wesson et al. [2004])

$$v = v_0 \left[1 - \left(\frac{r}{a}\right)^2\right]^\nu \tag{4.24}$$

is used. Typical values of ν are in the range $(1, 3)$.

Plot of profiles for various ν is shown in Fig. 4.1 (b).

4.4 Reconnection of magnetic lines

The magnetic system (it may consist from more subsystems), as all systems, tends to reach its energetic minimum. Magnetic lines of subsystems connect one to an other to reach such state. This spontaneous change of configuration of magnetic lines is called *magnetic reconnection*. Free energy heats plasma in its vicinity during magnetic reconnection.

The magnetic reconnection is a consequence of a magnetic diffusion; thus it can be described only by the resistive magnetohydrodynamics. Whether to use ideal or resistive MHD it can be determined by the *Lundquist number*

$$\#_{Lu} \equiv S \equiv \frac{\tau_R}{\tau_A} = L\rho\mu_0 v_A, \tag{4.25}$$

which is given by a fraction of *resistive time* and Alfven time. Resistive time characterise diffusion in the plasma. Diffusion is caused by final resistivity of the plasma. Alfven time is characteristic for most of changes in the plasma and it is given by Alfven velocity v_A, which is a typical velocity of ion low-frequency oscillations in the plasma (Kulhánek [2011]).

Lundquist number for tokamak plasma[2] is approximately $S = 10^8$. Resistive MHD becomes important just in cases of week magnetic fields; thus, ideal MHD can by used in the most of plasma volume and the resistive solution would be applied in resistive zones.

If the plasma has nonzero resistivity, magnetic lines aren't frozen in plasma and resistive MHD must be used. Plasma moves (drifts) perpendicularly to magnetic lines with velocity

$$\vec{v}_d = \eta \frac{\vec{j} \times \vec{B}}{B^2} = \eta \frac{\mathrm{rot}\, \vec{B} \times \vec{B}}{\mu_0 B^2}. \tag{4.26}$$

Reciprocal move of plasma cause its reconnection. Free energy heats the plasma with Joule heat. The point where the reconnection of magnetic lines happened is called *X-point*. In tokamak plasma at least two X-points are in the neutral area. So-called *magnetic islands* (*plasmoids*) are created between X-points. Centers of islands are called *O-ponts*. Different topologies of magnetic lines are separated with curve a called *separatrix*[3] (see Fig. 4.2).

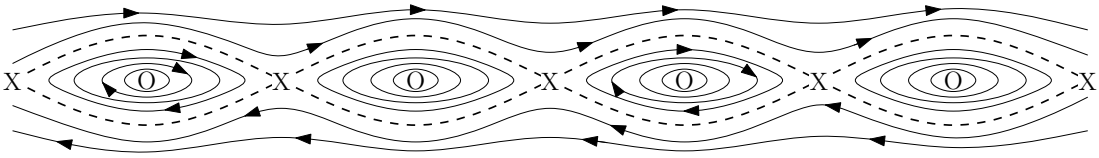

Figure 4.2: Reconnection of magnetic lines. Magnetic lines reconnect in X-point. Magnetic islands with O-points in the center are between X-points. Dashed line represents separtrix, which separates different topology of lines.

The *reconnection index*[4] is used for estimation of speed of reconnection. Reconnection index is defined as a ratio of plasma and Alfven speeds

$$\#_{sp} = \frac{v_d}{v_A} \approx \frac{1}{S}. \tag{4.27}$$

The Lundquist number is high for tokamak plasma and the reconnection index is small; thus the rate of spontaneous reconnection is small and another mechanism of reconnection should exist. Instabilities caused by reconnection are called *tearing instabilities*. Reconnection on tokamaks in a high β plasma is mainly

[2] with characteristic size of system $L = 1\,\mathrm{m}$

[3] Don't confuse this separatrix with separatrix of whole plasma.

[4] also called Alfven Mach number

triggered by neoclassical diffusion (see Sec. 1.3.3); that is why this instability is called *neoclassical tearing modes* (NTM).

4.5 Grad–Shafranov equation

The equilibrium of an axisymmetric system such as tokamak can be described by *Grad–Shafranov equation*. It is differential equation for the poloidal flux function ψ

$$R\frac{\partial}{\partial R}\frac{1}{R}\frac{\partial\psi(R,z)}{\partial R}+\frac{\partial\psi(R,z)}{\partial z}=-\mu_0R^2\frac{\partial p(\psi)}{\partial\psi}-\mu_0^2f(\psi)\frac{\partial f(\psi)}{\partial\psi}. \tag{4.28}$$

This is PDE involving $\psi(R,z)$, $f(\psi)$ and $p(\psi)$. It is used to interpret tokamak's shots or to design experiments. This equation cannot be solved analytically in general.

There are two ways how to solve this equation (Dudson [2011])

- Forward codes, which calculate equilibrium of $\psi(R,z)$ from known $f(\psi)$ and $p(\psi)$ functions. This class is used mainly by theorists.
- Interpretive codes, which take experimental data and work out the equilibrium. This way is used to interpret shots. Example of method from this class is *EFIT*, which is used on Compass tokamak.

As a consequence of Eq. 4.28 the plasma center is shifted towards outboard with respect to geometrical center of vessel. This shift is so-called the *Shafranov shift*. The Shafranov shift is shown in Fig. 5.8 on page 48.

5. MHD instabilities

5.1 MHD stability

The majority of the strongest instabilities in a simple form can be described with the MHD model. MHD instabilities usually occur on magnetic surfaces with rational value of $q = m/n$, with short connection length. The system naturally tends to its stability. The energetic perturbation of the plasma system can be described by (Dudson [2011])

$$\delta W_p = \frac{1}{2}\int \mathrm{d}^3x \tag{5.1a}$$

$$\Bigg[+ \frac{|\vec{B}_1^2|}{\mu_0} \qquad \text{Field-line bending} \geq 0 \tag{5.1b}$$

$$+ \frac{B^2}{\mu_0}|\operatorname{div}\vec{\xi}_\perp + 2\vec{\xi}_\perp \cdot \vec{\kappa}|^2 \qquad \text{Magnetic compression} \geq 0 \tag{5.1c}$$

$$+ \gamma p_0 |\operatorname{div}\vec{\xi}|^2 \qquad \text{Plasma compression} \geq 0 \tag{5.1d}$$

$$- 2(\vec{\xi}_\perp \cdot \operatorname{grad} p)(\vec{\kappa} \cdot \xi_\perp^*) \qquad \text{Pressure/curvature drive, + or } - \tag{5.1e}$$

$$- \vec{B}_1 \cdot (\vec{\xi}_\perp \times \vec{b}) j_\parallel \Bigg] \qquad \text{Parallel current drive, + or } -, \tag{5.1f}$$

where $\vec{\xi}(\vec{r})$ is *displacement* defined as a distance that the fluid moved from its equilibrium, $\vec{\kappa}$ is a center of curvature and $\vec{B}_1$ perturbed magnetic field. If the variation of potential energy is positive, system is stable.

First three terms of equation (5.1) determine stability. The stabilizing effects are illustrated in Fig. 5.1 and 5.2. Between stabilizing effects belong *magnetic field-line bending*, *magnetic compression* and *plasma compression*. If the center of curvature is in the opposite direction to the plasma pressure gradient[1] ($\vec{\kappa} \cdot \nabla p < 0$) then the plasma is also stabilized by a *good magnetic field curvature*. Last mentioned effect is driven by term. (5.1e).

The case of *bad curvature* ($\vec{\kappa} \cdot \nabla p > 0$) leads to instability driven by plasma pressure called *interchange instability*.

The pressure profile of plasma has its maximum near to center of the vacuum vessel. Due to the toroidal geometry, the good curvature occurs on inboard side

[1] This case is called *good curvature*.

of the vessel and the bad curvature on outboard. As a consequence, so-called *ballooning* type modes appear with amplitude maximum on outboard side.

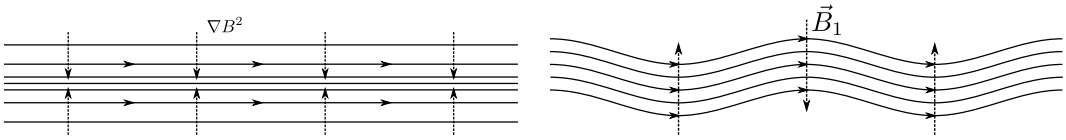

(a) (b)

Figure 5.1: Stabilizing effects of magnetic field line compression (a) and magnetic field bending (b).

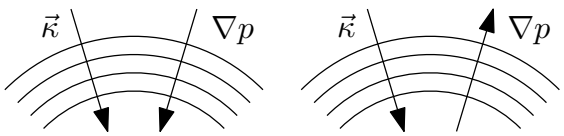

(a) (b)

Figure 5.2: Bad curvature (a) and good curvature (b). The case of good curvature stabilize the plasma.

Previous described instabilities belong to so-called pressure driven instabilities leaded by the term (5.1e). Other instabilities are driven by parallel current leaded by term (5.1f). These instabilities are typical for low values of β when the magnetic pressure is dominant.

Examples of basic MHD instabilities driven by magnetic pressure are kink and sausage instabilities shown in Fig. 5.4. The observation of these instabilities is typical mainly for Z-pinch discharges; however,they can be precursors of other MHD instabilities in tokamak. Using Ampère's law for current tube gives

$$\vec{B} = \frac{\mu_0 I}{2\pi r}.$$

Thus the magnetic pressure is proportional to

$$B^2 \propto \frac{1}{r^2}.$$

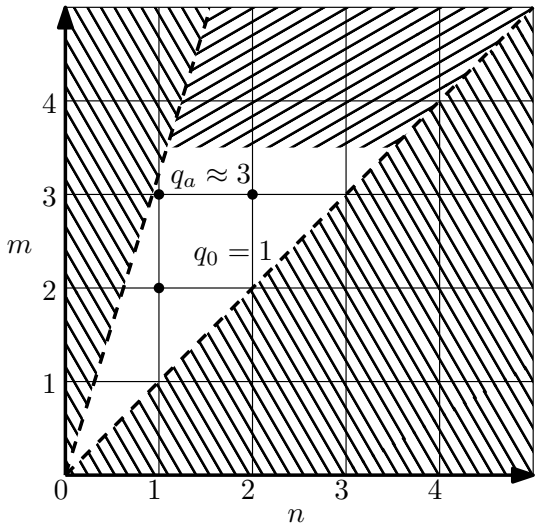

Figure 5.3: Determining possible mode numbers of potential instabilities. Modes are restricted with $q_0 < m/n < q_a$ and with a stability for higher m at low β.

Let's consider a homogeneous current tube. This current tube is in MHD equilibrium. However, when the perturbation in width of tube appears (Fig. 5.4 (a)) the magnetic pressure increases in the location of the perturbation and supports the growth of the instability. This mechanism leads to so-called *sausage instability* (Dudson [2011]). Similar mechanism leads to the *kink instabilities* (Fig. 5.4 (b)). If the current tube is curved, the magnetic pressure increases at the inner region and decreases at the outer region. This change in magnetic pressure leads to the instability. Internal kink $m = 1$ instability is a precursor for the resistive type sawtooth instability. Resonant instabilities are typical for rational q surfaces where field line bending is minimized due to resonant conditions (Dudson [2011]). To the category of resonant instabilities belongs also tearing mode instability that is described separately in Sec. 5.3

5.1.1 Disruption

Unexpected loss of the plasma confinement is known as a disruption. This event is mostly characterised by a sudden loss of the plasma current and a sudden drop of temperature. However, disruption is well seen by almost all detectors.

During the disruption, there is a big amount of loosen electromagnetic energy. This energy is loosen in the explosion in the vessel and by production of runaway

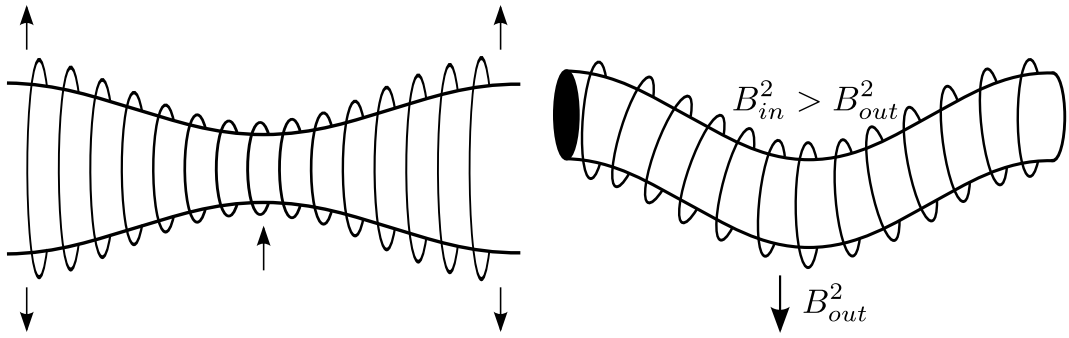

(a) (b)

Figure 5.4: Two basic types of ideal MHD plasma instabilities observed during Z-pinch discharges. (a) The sausage $m = 0$ instability isn't for typical for tokamaks; however, the kink $m = 1$ instability is observed as a precursor of sawtooth instability, which is resistive type of MHD instability.

electrons. This high energy electrons cause erosion of tokamak vessel. Thus, disruptions on large tokamaks are very unwanted.

Disruption can be triggered by various physical events, a lot of them is discussed in (Wesson et al. [2004]). Disruption process can be divided into four phases. Pre-precursor, precursor, fast and quench phase. Typical behaviour is shown in Fig. 5.5 (a).

The underlying change leads to growing of unstable configuration during the *pre-precursor phase*. As soon as the underlying change reaches a critical point an onset of MHD instability starts. *Precursor phase* is usually connected with growing magnetic oscillations of $m = 2$ mode. Typical duration of this phase is $\sim 10\,\mathrm{ms}$. During the *fast phase* the plasma reaches a second critical point and the rapid collapse of central temperature follows on a timescale of the order of milliseconds. The rapid fall of current gives rise to a characteristic short negative voltage pulse. Finally, the *quench phase* is characterised by a relatively fast current decay. The decay time depends on the particular conditions (see for example Fig. 5.5 (b)).

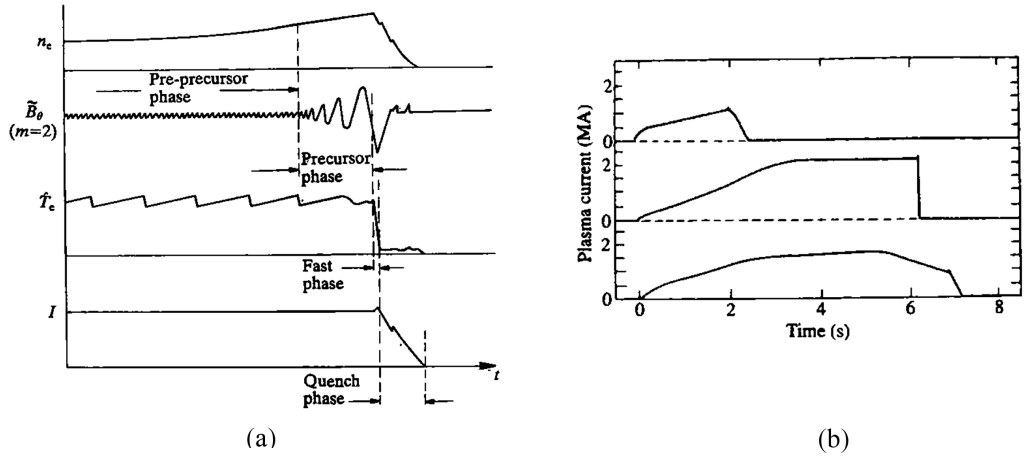

Figure 5.5: (a) Typical time dependence of the plasma density, $m = 2$ magnetic fluctuations, central temperature and plasma current during the disruption. (b) Time dependencies of the plasma current showing disruption during rise-up, flat-top phase and current fall (JET). This Figure is taken from (Wesson et al. [2004]).

5.2 Sawtooth instability

5.2.1 Theory

Sawtooth instability have been first observed by von Goeler et al. [1974] on ST tokamak in 1974. The instability can be seen as a sawtooth pattern on SXR signal. The origin of instability is localized on the $m = 1$ and $n = 1$ magnetic surface.

First theoretical explanation has been given by Kadomtsev [1975] in the year 1975. The Kadomtsev's model gives an intuitive explanation of sawtooth oscillations. However, this model has been inconsistent with further observations of q-profile after crash (Imríšek et al. [2013]). New models by (Porcelli et al. [196]) and (Zakharov et al. [1993]), which improve the Kadomtsev's model, have been presented recently.

According to Kadomtsev's model, the slow heating of plasma in the center is followed by sudden cool down; whilst the plasma in outer region is heated up. The plasma in the region surrounded by $q = 1$ rational surface is displaced and the second magnetic island is formed. As the magnetic island growth it partially surround the hot core which is then expelled to the edge. The existing magnetic

island takes place of new plasma core and the process is repeated. The formation of sawtooth instability is shown in Fig. 5.6

Sawtooth instability is characterized by typical "sawtooth" signal of SXR detector. In agreement with Kodomtsev model, signal from the plasma edge is inverted with respect to clear sawtooth signal from the plasma core. The signal inversion happen on so-called *inverse radius*, where the temperature remain roughly constant.

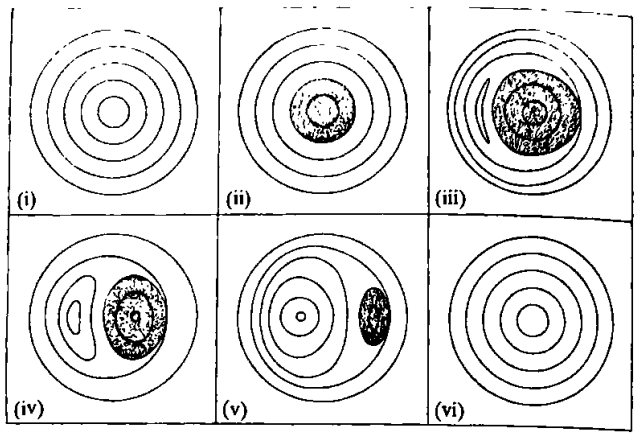

Figure 5.6: Development of magnetic field structure during the sawtooth in specific poloidal cross section.

Controlling of sawtooth seems to be very important for the future tokamaks. The impurities from the fusion could be removed form the plasma core by short period sawtooth oscillations. It has been shown (Chapman [2011]) that the sawtooth could trigger transition from L-mode to H-mode. On the other hand, long period sawtooth oscillations seed other MHD instabilities and; as a consequence, decrease plasma confinement. Sawtooth oscillations are potentially dangerous mainly during the period of thermonuclear fusion because of produced alpha particles, which lead to dangerous longer sawtooth period. Sawtooth instabilities can be stabilized and (or) controlled (Chapman [2011]) by electron cyclotron current drive (ECCD), ion cyclotron resonance heating (ICRH) and counter current neutral beam injection (NBI) (Chapman et al. [2007]).

5.2.2 Illustration of sawtooth instability on the Compass tokamak

Sawtooth oscillations can be illustrated on shot 4155. The plasma was vertically elongated to the elliptical shape during this shot. The shot has relatively long flat top phase and ends with disruption caused by mode locking. The signal from SXR-A detector is shown in Fig. 5.7. The sawtooth signal is most evident on signals from the plasma center, e.g. channels 21 – 28. As detector chord approaching $q = 1$ surface, the sawtooth signal is less dominant. Unfortunately, the inverse sawtooth signal haven't been observed by any SXR detector due to its weakness.

Sawtooth oscillations frequency has been determined as approximately (400 ± 20) Hz. The inverse radius has been observed by channels 18, 19 on one side and by channels 32, 33 on the other side. If the geometry of SXR chords is plotted together with EFIT magnetic reconstruction, the approximate position of $q = 1$ surface can be determined (see Fig. 5.8 (a)). In Fig. 5.8 (b) EFIT reconstructed q-profile is shown. The EFIT inaccuracy is clearly visible from q-profile reconstruction. Even the lowest q value doesn't occur below the value $q = 1$. However, the $q < 1$ value in the plasma center is consequence of the sawtooth occurrence. The EFIT error is approximately 10 % (Imríšek et al. [2013]) in determining of q_0.

Shafranov shift of the plasma center is clearly visible on the EFIT reconstruction. The Shafranov shift leads to the asymmetry of q-profile (see Fig. 5.8 (a) and (b)).

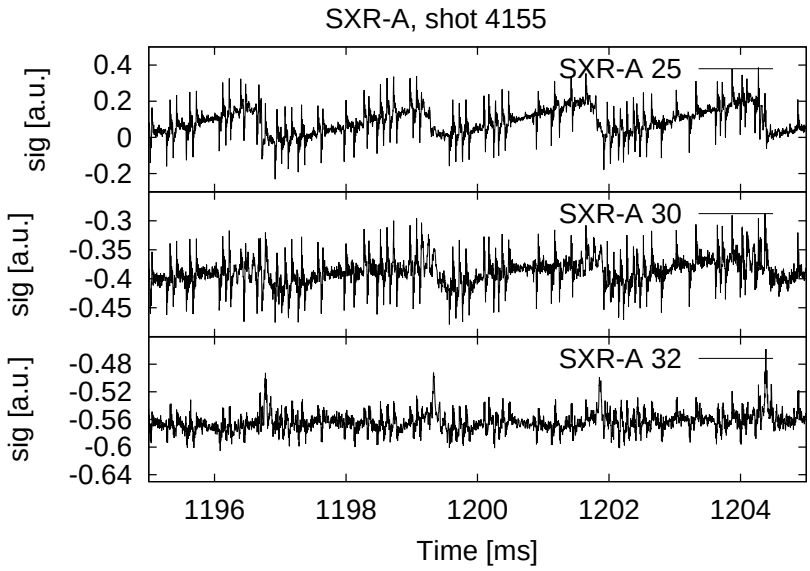

Figure 5.7: On the SXR signal from detectors 25, 30 and 32 are clearly visible sawtooth oscillation. The strongest oscillation are visible in the plasma center (detector 25) and become weaker to inverse ratio (detectors 30 and 32).

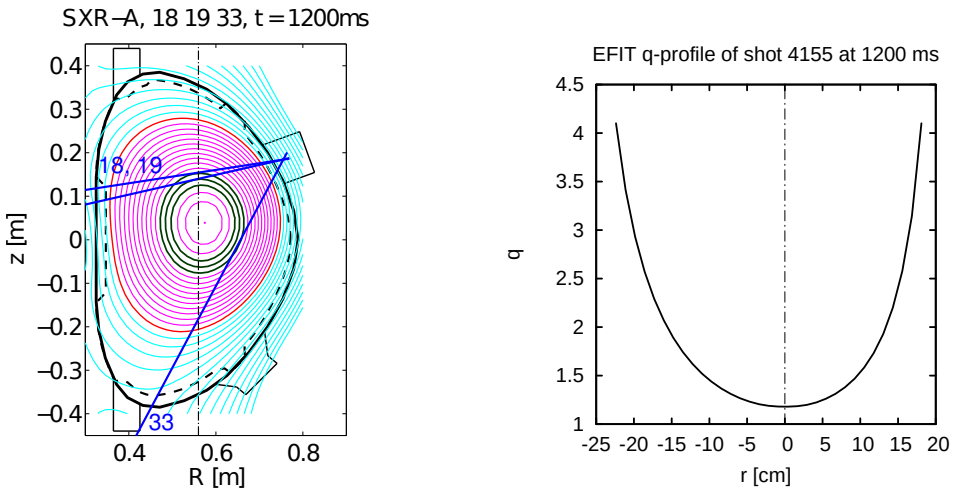

(a) (b)

Figure 5.8: (a) Geometry of SXR-A detector and chords of channels 18, 19 and 33. Contours connect places with the same value of q (from EFIT). The plasma is in the region of purple lines. The green contours refer to inverse radius (see Fig. 5.7). (b) Radial q-profile from EFIT reconstruction.

5.3 Theory of tearing modes

5.3.1 Magnetic islands

The magnetic lines are frozen in the plasma in an ideal MHD and the particles follow magnetic lines. However, on surfaces with high values of toroidal or poloidal modes (m, n) particles on a particular magnetic surface dissipate to other plasma due to collisions on Larmor radius

$$R_L \equiv \frac{mv_\perp}{QB}. \tag{5.2}$$

Collisional energy dissipation is negligible on surfaces with rational values of $q = m/n$ with low values of m, n. Thus, these *resonant surfaces* are more susceptible to MHD instabilities.

Mechanism of a magnetic island formation has been described in Sec. 4.4. The frame of reference has to be understand with respect to the resonant surface with $q_s = m/n$, where the poloidal magnetic field is taken to be zero

$$B^* = B_\theta \left(1 - \frac{n}{m} q(r)\right). \tag{5.3}$$

Described geometry is shown in Fig. 5.9.

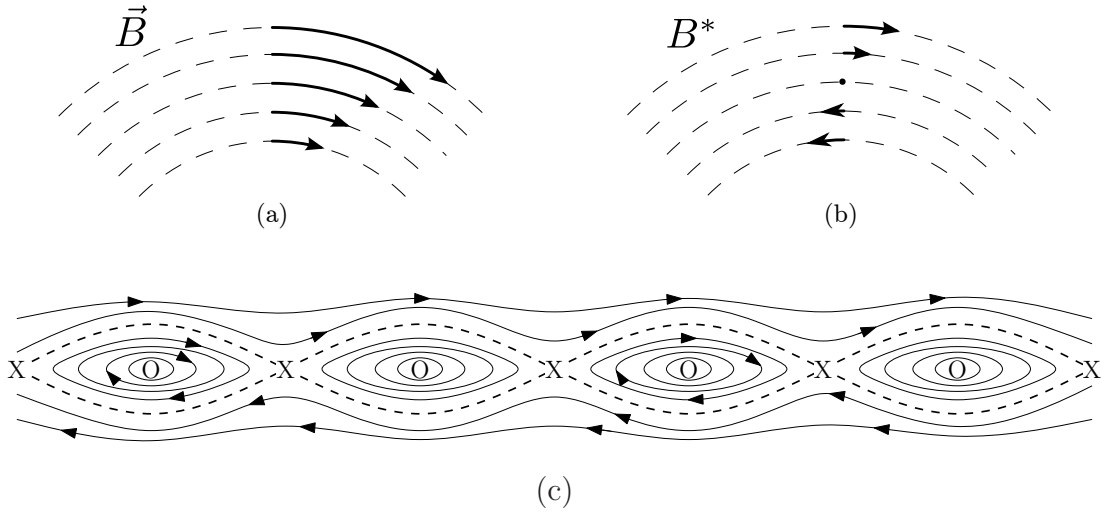

Figure 5.9: Poloidal geometry of magnetic field (a) and transformation to B^* (b). In the geometry shown in (b) magnetic curves can be teared and magnetic island (c) can occur.

In the view of resonant surface, the magnetic lines above and under resonant surface has opposite direction and reconnection can happen. Magnetic recon-

nection forms m magnetic islands in poloidal and n islands in toroidal direction. These island are helically stretched around the resonant surface.

Special case, so call *Mirnov instability*, happens during the current rise when the resonant surfaces are being thrown up due to the decreasing sequence of poloidal mode numbers. For large-aspect ratio circular plasma the decreasing value of q is related to the increasing plasma current with equation (1.18)

$$q_a = \frac{2\pi a^2 B_\phi}{\mu_0 I R}.$$

5.3.2 Classical theory of tearing modes

The tearing instability is a typical example of resistive MHD instability driven by parallel current (Eq. 5.1f). A finite resistivity of the plasma near to rational surfaces leads to radial drifts. These drifts and other MHD activity lead to tearing of the magnetic field lines and to tearing modes in the form of magnetic islands.

The resistivity in the most of the plasma volume is negligible and thus ideal MHD theory can be used. However, resistive MHD becomes important at the resonant surfaces. As a consequence, the ideal MHD theory involve solving a set of ideal MHD equations over the most of the plasma and another set of resistive MHD equations around the resistive layer.

Classical plasma drifts cause tearing of magnetic curves in a long time period. However, the time period is dramatically shorten by MHD activity.

Consequently, the growth or decay of the island width w is described by Rutherford equation (Wesson et al. [2004])

$$\frac{\mathrm{d}w}{\mathrm{d}t} \simeq \frac{r_s^2}{\tau_R}\Delta'(w), \tag{5.4}$$

where τ_R is local resistive time, r_s minor radius of rational surface and $\Delta'(w)$ is logarithmic jump of the radial magnetic field perturbation across the rational surface. In the linear approximation Δ' is taken to be constant. The meaning of Δ' is more discussed in the next section (Sec. 5.5).

Occurrence of the magnetic island or the group of non-overlapping islands lead to a local flattening of temperature and pressure profiles, which leads to degradation of plasma confinement (Haye [2006]).

Cylindrical tearing mode equation

Several assumptions have to be done to obtain the cylindrical tearing mode equation. By solving this equation a parameter Δ' can be obtained, this parameter describes the growth or decay of magnetic island width.

Following assumptions are included:

- Only small perturbations are assumed; thus, the linearization can be used and the $\vec{B}$ and $\vec{j}$ can be expanded to series

$$\vec{B} \cong \vec{B}_0 + \delta\vec{B}_1,$$
$$\vec{j} \cong j_0 + \delta\vec{j}_1,$$

  where δ is small positive number, $\vec{B}_1$ and $\vec{j}_1$ is some small perturbation to equilibrium vectors $\vec{B}_0$ and $\vec{j}_0$.

- Large aspect ratio ($\varepsilon = a/R \ll 1$) approximation is done; thus it can be written

$$B_\theta \sim \frac{1}{r}\frac{\mathrm{d}B_\phi}{\mathrm{d}r} \sim \varepsilon B_\phi,$$
$$j_\theta \sim \varepsilon j_\phi$$

  for appropriate perturbations

$$B_{\theta 1} \sim \varepsilon B_{r1} \sim \varepsilon B_{\phi 1},$$
$$j_{\theta 1} \sim j_{r1} \sim \varepsilon j_{\phi 1}$$

- A cylindrical approximation is used and the relation

$$q = \frac{rB_\phi}{RB_\theta}$$

  is used in derivation of cylindrical tearing mode equation.

- The perturbation is taking to have the form $\propto \mathrm{e}^{i(m\theta - n\phi)}$ and partial derivations can be substituted $\partial/\partial\theta \to im$ and $\partial/\partial\phi \to -in$.

Using these assumptions and ideal MHD theory, the *cylindrical tearing mode equation* can be written is a form (Wesson et al. [2004])

$$\frac{1}{r}\frac{\mathrm{d}}{\mathrm{d}r}r\frac{\mathrm{d}\psi}{\mathrm{d}r} = \frac{m^2}{r^2}\psi - \frac{\mathrm{d}j_\phi/\,\mathrm{d}r}{\frac{B_\theta}{\mu_0}\left(1 - \frac{nq}{m}\right)} = 0. \tag{5.5}$$

Equation (5.5) has a singularity at resonant surface $r = r_s$, where $q = m/n$. Thus, the equation has to be solved with appropriate boundary conditions in region $r < r_s$ and $r > r_s$ separately. The expected function $\psi(r)$ is continuous in its value, but not necessarily continuous in its first derivative; thus, the parameter Δ' is defined as

$$\Delta'(0) \equiv \Delta' = \frac{\psi'}{\psi}\bigg|_{r=r_s-\delta}^{r=r_s+\delta} \qquad \delta \to 0. \tag{5.6}$$

The meaning of Δ' gives resistive MHD theory and it determines island growth through the Rutherford equation (5.4) and (5.20).

Numerical solution of Cylindrical Tearing Mode equation

Let's expand Eq. (5.5) on resistive surface. Substituting the term (Wesson et al. [2004])

$$\left(1 - \frac{nq}{m}\right) \to -\left(\frac{q'}{q}\right)_{r_s} (r - r_s)$$

and keeping the dominant terms, Eq. (5.5) becomes

$$\frac{\mathrm{d}^2\psi}{\mathrm{d}s^2} - \frac{\kappa}{s}\psi = 0, \tag{5.7}$$

where $s = r - r_s$ and $\kappa = -(\mu j' q/B_\theta q')_{r_s}$. Equation (5.7) has a singularity at $s = 0$ and has to be solved on region $s < 0$ and $s > 0$ separately. The expanded solution or Eq. (5.7) taking form Wesson et al. [2004]

$$\psi = 1 + \kappa s \ln|s| + \cdots + A^- s + \cdots \qquad r < r_s, \tag{5.8}$$

$$\psi = 1 + \kappa s \ln s + \cdots + A^+ s + \cdots \qquad r > r_s, \tag{5.9}$$

where A^- and A^+ are constants, which have to be determined. This solution is continuous at $s = 0$. Derivatives of the Eq. (5.8) and (5.9) now taking a form

$$\psi' = \kappa \ln|s| + \kappa + A^-, \qquad r < r_s, \tag{5.10}$$

$$\psi' = \kappa \ln s + \kappa + A^+, \qquad r > r_s. \tag{5.11}$$

The derivative of ψ has a jump at $s = 0$. Calculation of Δ' gives

$$\Delta' = A^+ - A^-. \tag{5.12}$$

Now, the numerical calculation of Δ' with appropriate boundary conditions is obvious. Numerical calculation can be started at $s = 0$ with an appropriate

value of derivative given by (5.8) – (5.11). The calculation should ends at $r = 0$ in one case or at $r = a$ in the second case. Values of A^+ and A^- should be fitted to satisfy given boundary conditions. The value of constants can be found iteratively.

Boundary conditions

The boundary condition of Eq. (5.5) satisfies the regularity condition for $r = 0$ is $\psi = 0$.

The outer boundary condition depends on the position of the plasma edge and on the position and material of vacuum vessel. The geometry of the problem is presented in Fig. 5.10. There are following possibilities for the boundary region (Wesson et al. [2004]):

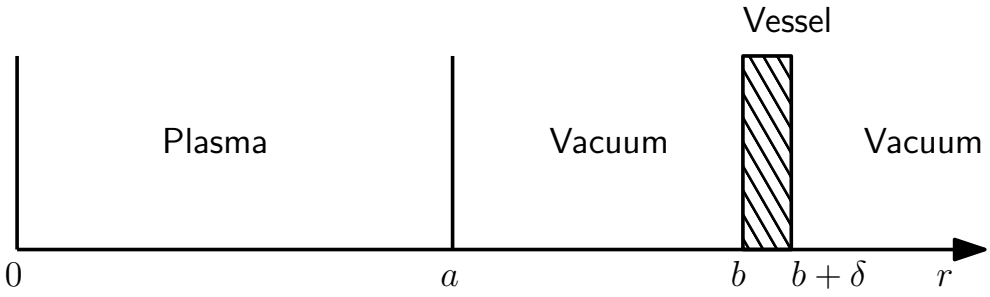

Figure 5.10: Geometry for the outer boundary condition of Eq. (5.5).

- The conducting shell is at the surface of the plasma. Then the boundary condition takes the form

$$\psi'(a) = \left(-\frac{m}{a} + \gamma\mu_0\rho\delta\right)\psi(a), \tag{5.13}$$

  where γ is the growth rate, σ is the conductivity of the shell and δ its thickness. There are two limit cases for σ.

  - The limit $\sigma \to \infty$ means a perfectly conducting shell and the boundary condition becomes

$$\psi(a) = 0. \tag{5.14}$$

  - For the case of the limit $\sigma \to 0$ the shell becomes to be an isolator and boundary condition gives

$$\psi'(a) = -\left(\frac{m}{a}\right)\psi(a). \tag{5.15}$$

On the Compass tokamak, the vacuum vessel is made of inkonel and thus well conducting. Discharges with a circular or elliptic shaped plasma, that are analysed in this thesis, are in continuous contact with the vessel. Thus, the $\sigma \to \infty$ assumption can be used in the case of Compass tokamak as the first approximation.

- The plasma volume ends in front of the vessel shell. The space between the plasma and the vessel is filled with vacuum. The solution of Eq. (5.5) has a form

$$\psi = Cr^m + Dr^m, \quad a < r < b \tag{5.16}$$

in the first vacuum region and in the second vacuum region a form

$$\psi = Fr^{-}m, \quad b + \delta < r < \infty. \tag{5.17}$$

Considering this form of the solution and taking the approximations

  - $\delta \ll b/m$ and
  - time dependence in a form $\exp(-i\omega t)$, where ω is tearing mode frequency,

the boundary condition becomes (Wesson et al. [2004])

$$\psi'(a) = -\frac{m}{a}\frac{1 + f(a/b)^{2m}}{1 - f(a/b)^{2m}}\psi(a), \tag{5.18}$$

the parameter f is defined as

$$f = \frac{1}{1 + (im/\omega\tau_s)}; \qquad \tau_s = \frac{\mu_0 \rho b \delta}{2}, \tag{5.19}$$

where τ_s is the characteristic resistive time constant of the shell, which is approximately $\tau_s \approx 210\,\mu$s (Gates et al. [1997]) for Compass tokamak.

  - A high frequency plasma perturbations implies decreasing penetration of the perturbations. The condition $\omega\tau_s \gg 1$ gives $f \to 1$ and $\psi(b) \to 0$. In this limit the shield behaves as a perfect conductor. (Wesson et al. [2004]).
  - For the limit (Nave and Wesson [1990]) $\omega\tau_s \to 0$, $f \to 0$ shell becomes invisible for the magnetic field. If $\omega = 0$ mode stops in plasma and according to its resistivity caused the plasma current decay and disruption.

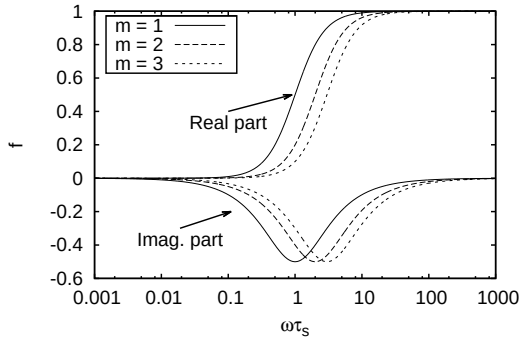

Figure 5.11: Real and imaginary parts of f from Eq. (5.19) for $m = 1, 2, 3$ as a function of $\omega\tau_s$.

Mode locking

At high frequencies wall behaves like perfect conductor. However as island grows there is a transfer of momentum between the plasma and the wall, which decrease the rotational frequency. Momentum is transferred mainly by mutual interaction between the plasma and the wall. The currents in the plasma and in the wall have shifted phases (Nave and Wesson [1990]).

The process of mode locking can be in simplification explained by use of f from Eq. (5.19) in analogy to absorbed wave. As the $\omega\tau_s$ is large, the imaginary part of f is negligible. However, if the $\omega\tau_s$ decreases the imaginary part of f will increase and as the mode will lost its phase velocity and therefore its frequency. Numerically calculated behaviour based on model of Nave and Wesson [1990] is shown in Fig. 5.12. An exponential decrease of plasma frequency and increase of perturbed magnetic signal during the mode locking can be seen.

Occurrence of the tearing modes degrades plasma confinement and slow plasma rotation can lead to *mode locking* with exponentially decreasing frequency and increasing penetration of the magnetic field to the wall (Nave and Wesson [1990]).

Neoclassical theory of tearing modes

Neoclassical tearing modes (NTMs) are resistive tearing mode islands which are sustained by a helically perturbed bootstrap current (Haye [2006]). In contrary to classical tearing modes, NTMs are high-beta phenomenon and occur even in

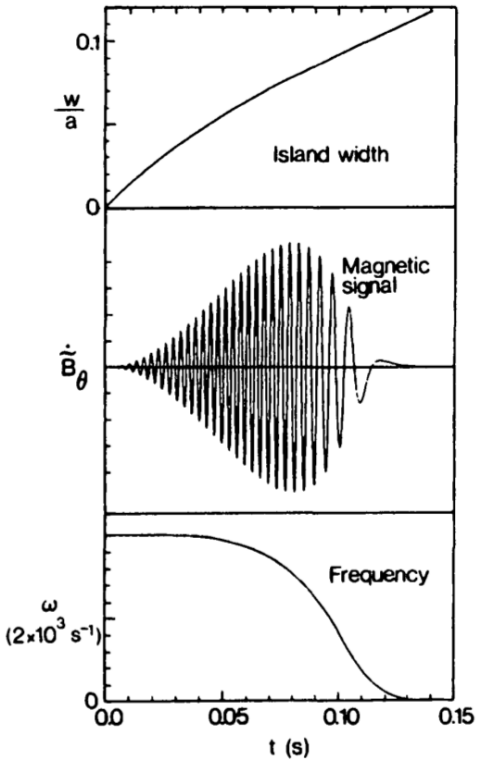

Figure 5.12: General behaviour during mode locking. The figure is taken from Nave and Wesson [1990].

a classically stable plasma.

The occurrence of magnetic islands leads to flattening of a plasma pressure profile. However, the gradient of pressure profile drives bootstrap current (see Sec. 1.3.3). Thus the bootstrap current disappears in O-points of island and remains in X-points.

Apart from helically perturbed bootstrap current, some other phenomena have to be mentioned to obtain final *modified Rutherford equation* (Haye [2006])

$$\frac{\tau_R}{r_s}\frac{\mathrm{d}w}{\mathrm{d}t} \simeq \Delta' r_s + \sqrt{\epsilon}\frac{L_q}{L_p}\frac{r_s}{w}\beta_p\left[\frac{w^2}{w^2+w_d^2} - \frac{w_{\mathrm{pol}}^2}{w^2}\right], \tag{5.20}$$

where L_q and L_p is a magnetic shear length $L_q = q/(\,\mathrm{d}q/\,\mathrm{d}r)$ and a pressure gradient length $L_p = -p/(\,\mathrm{d}p/\,\mathrm{d}r)$, w_d is an island threshold and w_{pol} polarisation threshold width. Thus, there are effects of transport threshold and polarisation threshold (Haye [2006]).

After the moving of Compass tokamak from UK to Czech Republic NTMs haven't been observed yet. However, the evidence of NTMs on Compass tokamak has been published in Gates et al. [1997] or Zohm et al. [1997].

5.4 Observation of tearing modes on the Compass tokamak

A general circular shot contains of three basic phases as it is seen in Fig. 5.13 (b). During a *ramp-up* phase the current is increasing. This phase is usually succeeded by Mirnov instabilities. After the ramp-up phase usually saturated *flat top* phase follows. The changes of current are minimal during this phase. Finally, the shot can end in a disruption caused by a mode locking or ends in a *ramp-down* phase succeeded by a self-healing mode.

For MHD analysis in this section discharges with circular or ellipse plasma have been chosen with typical plasma parameters $q_a = 2 - 3$, $\nu = 1.5 - 2.5$ and $\beta_N = 0.2 - 1$. The circular plasma is a subject to tearing modes at lower beta. The EFIT reconstruction works here[2] with reasonable error and with no need of data from additional diagnostics.

The tearing mode MHD activity on the Compass tokamak is detected by a wide range of diagnostics and techniques. The tearing modes are observed by measuring partial poloidal magnetic field, AXUV detectors, probe and Thomson scattering diagnostics directly and by measurement of parallel heat flux indirectly Weinzettl et al. [2013].

The magnetic island structure performs poloidal and toroidal rotations. A time development of combined[3] frequency can be measured by DTFFT. Island O-point moves along the magnetic coils, as the island poloidally rotates. The island movement can be reconstructed using the cross–correlation technique as is shown in Figs. 5.14 or 5.15. A poloidal mode number m, frequency and local poloidal angular velocity of island can be obtained from cross-correlation. A parity of toroidal mode number n can be obtained from correlation of the signal of two magnetic detector on one poloidal angle and on opposite toroidal angles. Such a pair of diagnostics is not currently working on the Compass tokamak; however, a combination of IPR and Mirnov coils, which are on nearly opposite toroidal angles, can be used[4].

[2] D-profiled plasma is more complex and thus more complicated for EFIT reconstructions.

[3] Combination of poloidal and toroidal rotations.

[4] See technical details in Sec. 2.1.

Mode number detection can becomes slightly difficult when groups of non-overlapping islands on different rational surfaces are obtained. The mode with higher q, which is generally closer to the plasma edge affects cross-correlation dominantly; however, the cross-correlation is affected with the lower q mode as well and the mode identification becomes more difficult. The mode number can be identified more precisely using q-profile from the EFIT reconstruction.

5.4.1 Mode locking

As a example of mode locking shot 4005 with mode lock at 2/1 and shot 4102 with mode lock at 3/1 rational surface have been chosen.

Shot 4005

The shot 4005 (see spectrogram in Fig. 5.13 (a)) is initiated by a sequence of $m = 5, 4, 3, 2$ Mirnov instabilities, as it is commonly observed on other tokamaks (Strait et al. [1989]). The Mirnov oscillations are followed by 2/1 tearing mode with slowly decreasing frequency. The mode is locked at the end with $q_a \approx 2$ and leads to a final disruption. From the signal in Fig. 5.13 (a) of perturbed magnetic field, the exponential growth of mode with an exponential decrease of the frequency is observed in a good agreement with the theory (Nave and Wesson [1990], Fig. 5.12).

Shot 4102

The mode lock in a circular plasma has been usually observed at 3/1 rational surface with $q_a \approx 3$. The shot is, as usual, initiated by Mirnov oscillations followed by saturated 3/1 tearing mode during the current flat top and is ended by a disruption.

Development of tearing mode of shot 4102 is shown at cross correlation graphs in Figs. 5.14, 5.15 and at spectrogram in Fig. 5.13 (b). The frequency of the oscillations is rapidly decreased at the beginning of mode (Fig. 5.15 (a), (b)) and then is slowly increasing to final mode lock ending with a disruption with $q_a \approx 3$. The decrease of frequency and a probable change of mode from $m = 3$ to $m = 2$ is shown in Fig. 5.15.

In Fig. 5.14 a comparison of Mirnov and IPR correlation signals are shown. The data from the Mirnov signal is much more noisy. The noise is seen in down part of the correlation figure. However, due to the bigger number of coils at HFS, the identification of mode number becomes more evident.

5.4.2 I_p scan

The behavior of the tearing modes with different plasma currents is well observable in shots 4707, 4708 and 4709. These shots differ only in preset values of the plasma current during the flat top phase. The basic plasma parameters are shown in Tab. 5.1. The spectrograms of these shots are shown in Fig. 5.18 (b) and Fig. 5.16. The tearing mode frequency is increasing with a decreasing plasma current; however, the amplitude of magnetic perturbations is decreasing. Thus, the plasma with the lower current is more stable to tearing modes.

This set of shots ends with a sudden increase of tearing mode frequency and gentle lost of the magnetic islands as it has been expected. This phenomenon is so-called *self-healing*. Here, the tearing mode is self-heal initiated by a start of ramp-down phase and continues during the ramp-down.

The perturbed magnetic field signal is shown in Fig. 5.17. A characteristic time of island growth is increasing with a decreasing plasma current. In the plasma with a higher plasma current, there is more available energy for reconnection; thus, the onset of tearing mode is faster and has a higher amplitude. The tearing activity in shot 4709, where is the lowest current from analysed shots, is almost unobservable. The mode amplitude is exponentially decreasing during the ramp-down phase. The amplitude decay consists of two phases in shots 4707 and 4708. This phenomenon is not fully understood. The value of q_a is increasing here; therefore, a temporary formation of new island can occur. However, this cannot be confirmed because of unreadable cross-correlation graphs. Unlike the mode onset, the characteristic time of mode decay is decreasing with the plasma current. This is caused by energy which have has freed during the mode growth.

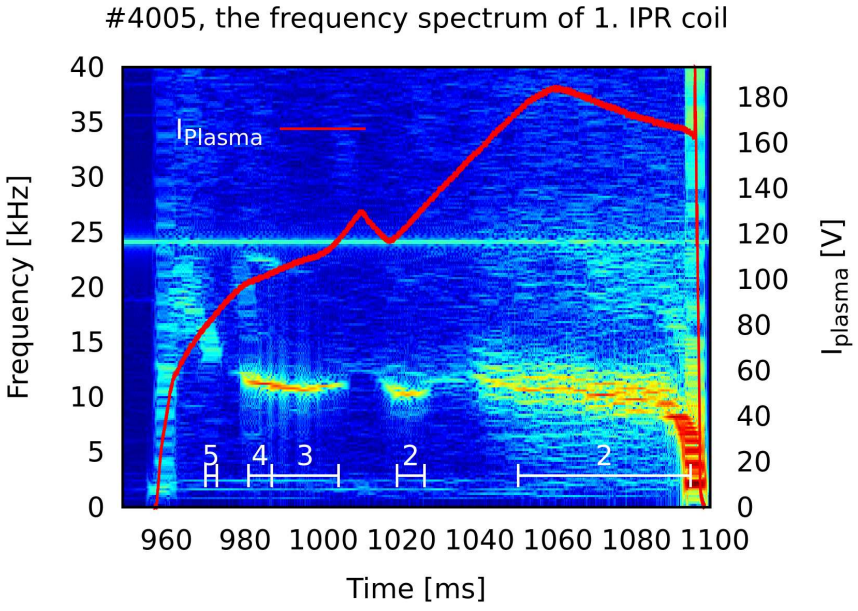

(a)

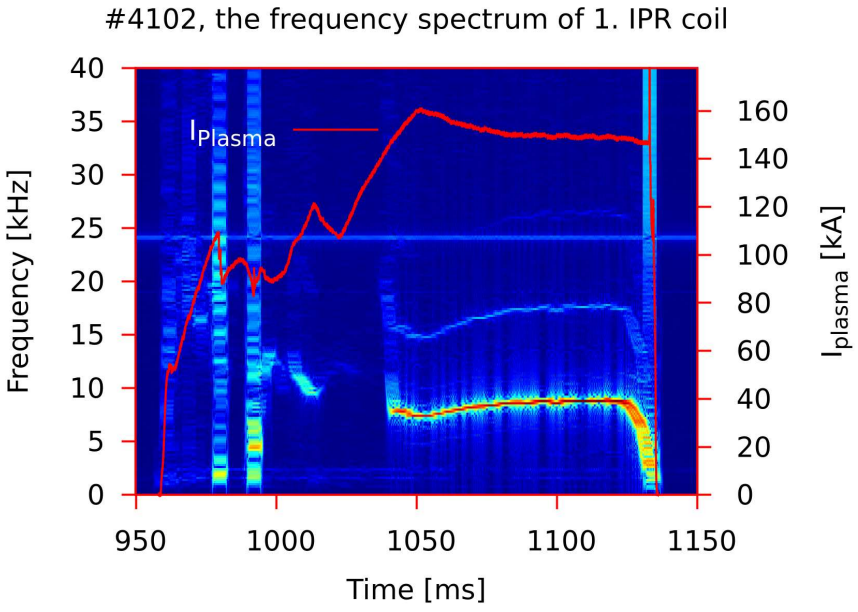

(b)

Figure 5.13: Spectrograms of shots 4005 (a) and 4102 (b). Both shots end with a disruption. The white numbers in the down part of the figure represent determined poloidal number m.

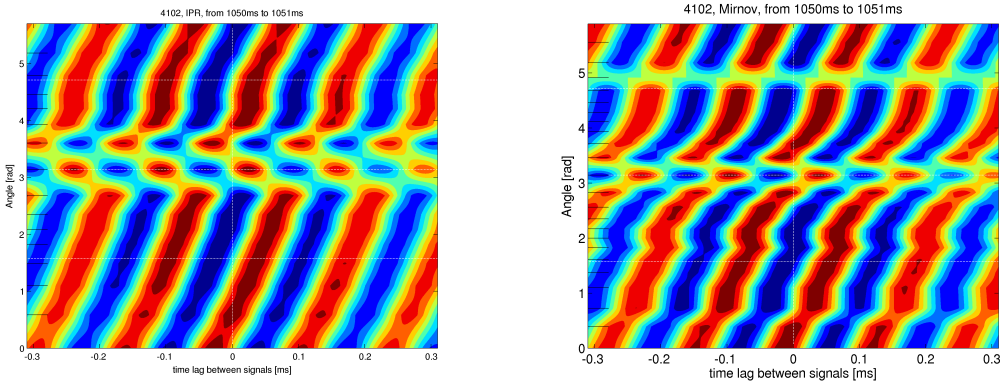

(a) (b)

Figure 5.14: Cross-correlation graphs from (a) IPR coils and (b) Mirnov coils. The signal is taken from shot 4102 in time 1050.1 ms.

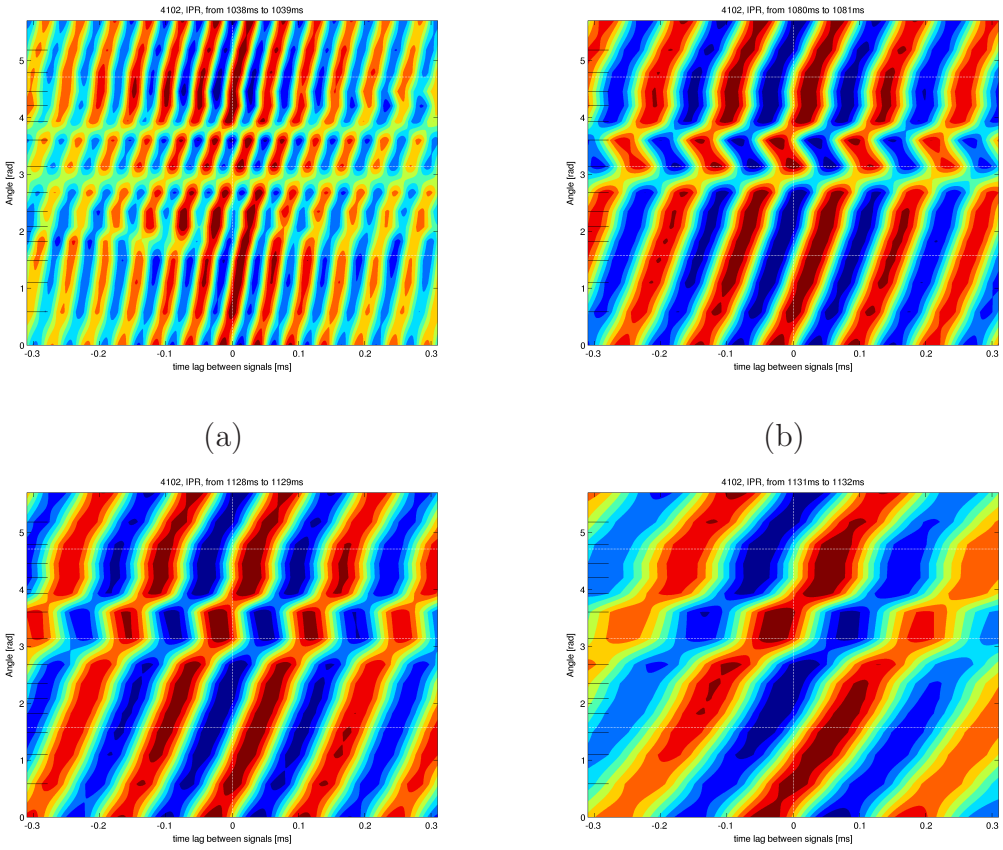

(a) (b)

(c) (d)

Figure 5.15: Cross-correlation graphs of shot 4102. On the sequence of figures (a) — (d) is seen a develop of the frequency and poloidal mode number m.

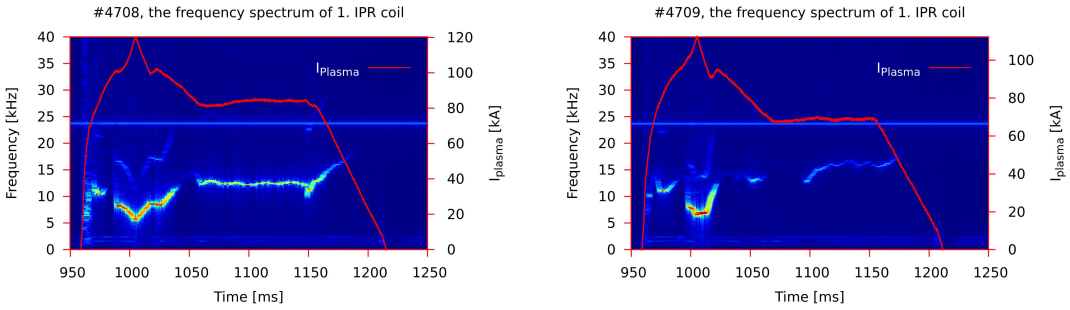

(a) (b)

Figure 5.16: Spectrograms of shots 4708 (a) and 4709 (b).

Shot	I_p **[kA]**	n $[\times 10^{19}\mathrm{m}^{-3}]$	β_N	β_p	f **[kHz]**
4707	102	2.56	0.53	0.25	9.6
4708	87	2.54	0.49	0.27	12.7
4709	72	2.49	0.56	0.38	15.7

Table 5.1: Parameters of plasmas during the flat top phase .

5.4.3 Influence of tearing mode activity on plasma parameters

The influence of tearing modes on plasma parameters can be illustrated on pair of shots 4706 and 4707. The shot 4706 is the first shot after glow discharge. Due to the glow discharge, a vacuum is cleared from impurities. In the shot 4706, suppression of tearing mode activity during flat top can be seen. In the next shot with the same settings as in shot 4706 tearing mode is again observed (see Fig. 5.18). The mode appeared in flat top phase of the shot 4707 have been determined as $m = 2$ mode based on Mirnov coil and probably $m = 4$ mode based on IPR coils. This disagreement can be explained by inner structure of the island which is also reveled by higher harmonics in spectrogram. This mode persist in self-healing phase during ramp-down. The same mode as in shot 4707 then appears during current ramp-down.

Both discharges has a fast ramp-up phase and relatively long flat-top ended by ramp-down without disruption. The change in the current on the end of the discharge leads to increase of frequency and to exponential decay as is discussed

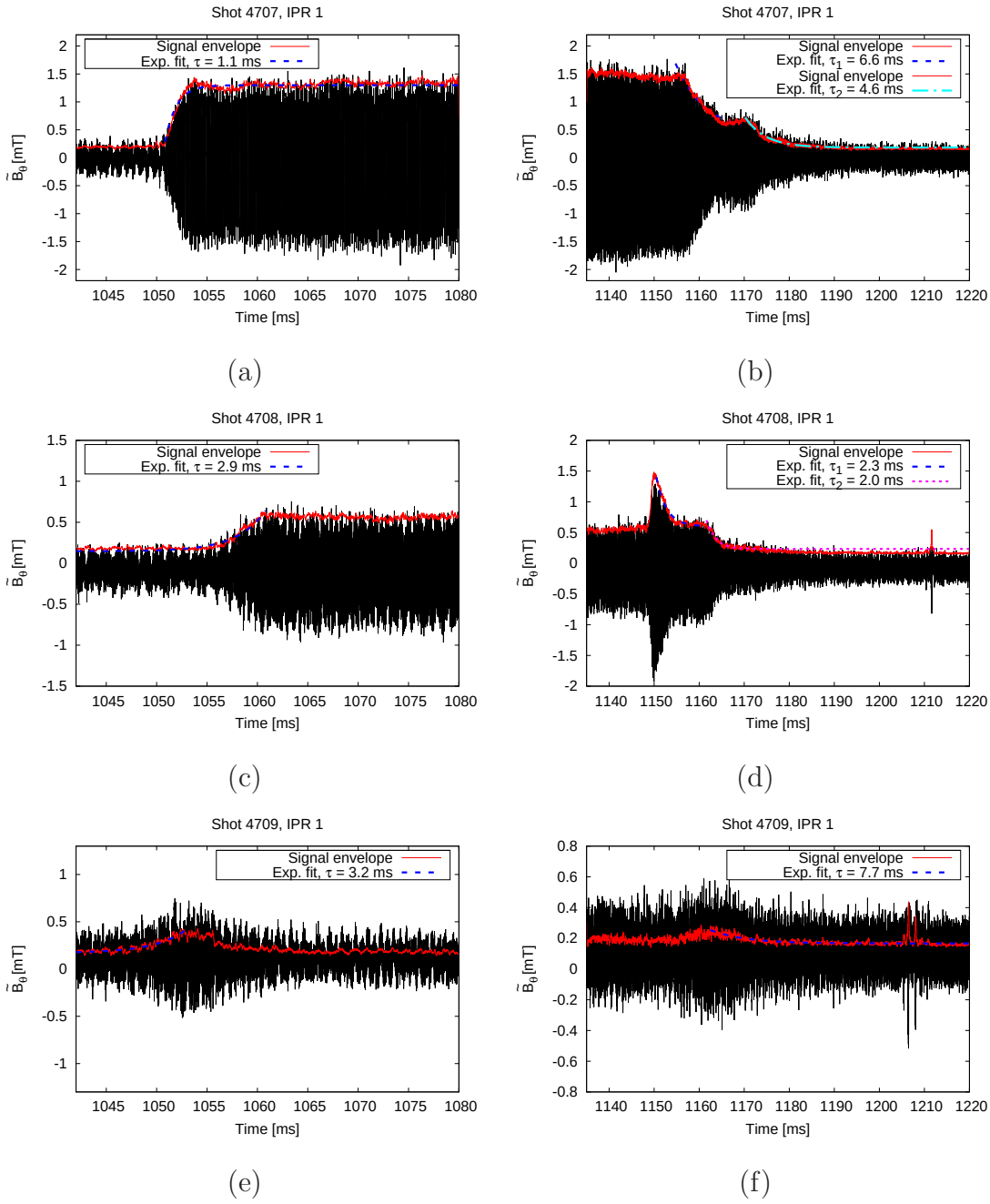

Figure 5.17: The signal of perturbed magnetic field of mode onset and mode decay. It is presented a sequence of shots 4707, 4708 and 4709 with the decreasing plasma current.

in Sec. 5.4.2. The sudden change of the plasma current on the end of the flat-top phase of shot 4706 leads to magnetic reconnection and sudden occurrence of MHD activity with same behavior as in shot 4707.

The consequences of MHD activity are seen in Fig. 5.20. The presence of tearing modes leads to degradation of confinement time and decrease of energy stored in the plasma. The tearing modes lead to parallel heat flux profile flattening near separatrix as is shown in Fig. 5.20 (b). The parallel heat flux is measured by IR cameras positioned to watch HFS limiter.

5.4.4 NBI versus no NBI

The influence of neutral beam injection (NBI) can be illustrated on shots 4786 and 4787. The NBI on shot 4786 is applied from time 1110 ms to 1130 ms. Exponential dissipation of MHD activity and small change of frequency is observed in Figs. 5.22 and 5.21 (a) if the NBI is applied. The spectrogram of the discharge with the same parameters but without a NBI is shown in Fig. 5.21 (b).

Not perfectly centralized and approximately $7-8$ cm wide NBI injection beam heat the plasma and flatten current profile; thus, the condition of island formation on rational surfaces disappear, as well as the tearing mode. After end of NBI injection stability persist for a while. During this period, the magnetic structures are stabilized until the next magnetic reconnection and the tearing mode activity occur. The characteristic times of mode decay and mode growth are similar.

5.4.5 Mode locking vs. self-healing analysis

The analysis of plasma conditions shortly before mode locking or at the end of flat top which initiated self-heal has been performed. The analysis has been done separately for each mentioned kind of a discharge to find a threshold between a mode locking and a self-heal. Shots with a circular plasma have been used. Analysed shots are presented in Tab. 5.2 and 5.3.

It has been found that low-q plasmas are more susceptible to mode locking. It has been shown (see Fig. 5.23) the average plasma density is important parameter in circular plasma. The low density plasma seems to be more stable to mode

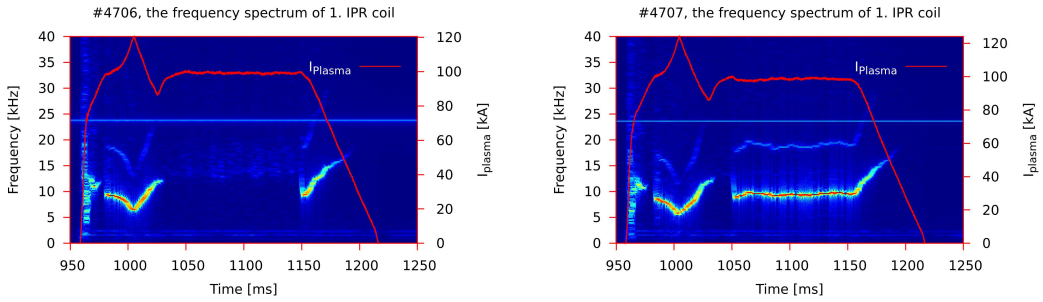

(a) (b)

Figure 5.18: Spectrograms of afterglow shot 4706 and shot 4707 with the same discharge settings.

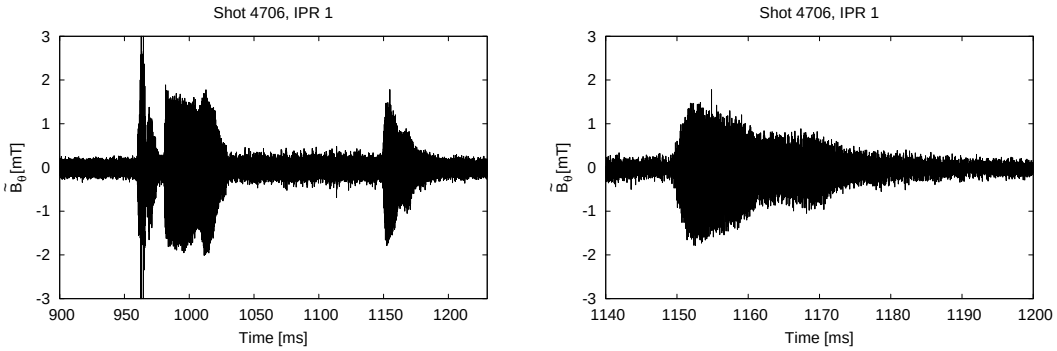

(a) (b)

Figure 5.19: (a) Signal of perturbated magnetic field of shot from the first IPR coil. (b) Detail of self-healing phase.

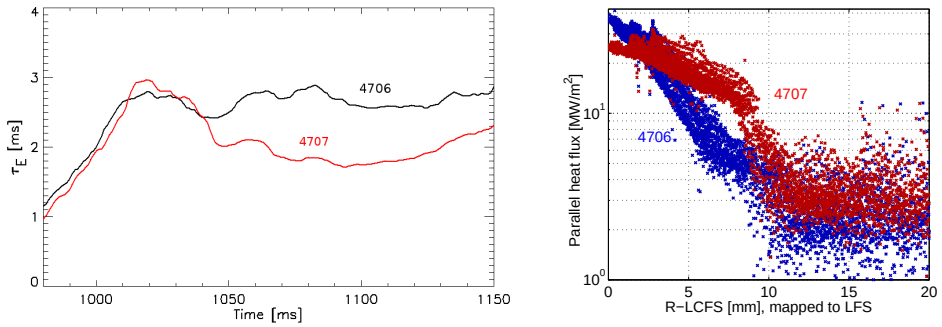

(a) (b)

Figure 5.20: The plasma confinement time (a) and parallel heat flux (b) observed by IR camera in shots 4706 and 4707. MHD activity leads to degradation of plasma performance and to flattening of parallel heat flux current. The figures are taken from Weinzettl et al. [2013]

locking as well as the low β_N plasma. The threshold for q_0 and q_a is clearly visible in the Fig. 5.23 (b).

The presented results are in a good agreement with earlier articles on Compass-D tokamak[5] (Gates et al. [1997], Zohm et al. [1997]) and other tokamaks (Haye [2006], Hegna and Callen [1994]).

Shot	I_p **[kA]**	n $[\times 10^{19}\mathrm{m}^{-3}]$	f **[kHz]**	**Shape**
4101	151	1.70	8.0	Circular
4108	151	2.07	8.2	Circular
4109	151	2.92	8.4	Circular
4707	102	2.56	9.6	Circular
4708	87	2.54	12.6	Circular
4712	95	2.09	8.7	Circular
4723	65	1.81	14.8	Circular
4724	65	2.64	14.7	Circular

Table 5.2: List of shots ending with self-healing used for analysis.

Shot	I_p **[kA]**	n $[\times 10^{19}\mathrm{m}^{-3}]$	f **[kHz]**	**Shape**
4005	187	6.16	10.2	Circular
4102	151	3.83	8.9	Circular
4103	150	3.70	8.4	Circular
4110	151	3.69	8.5	Circular
4111	152	3.61	8.9	Circular
4117	151	3.60	9.1	Circular
4696	95	2.79	7.3	Circular
4727	79	2.30	10.9	Circular

Table 5.3: List of shots ending with mode locking used for analysis.

[5] During its period in Britain

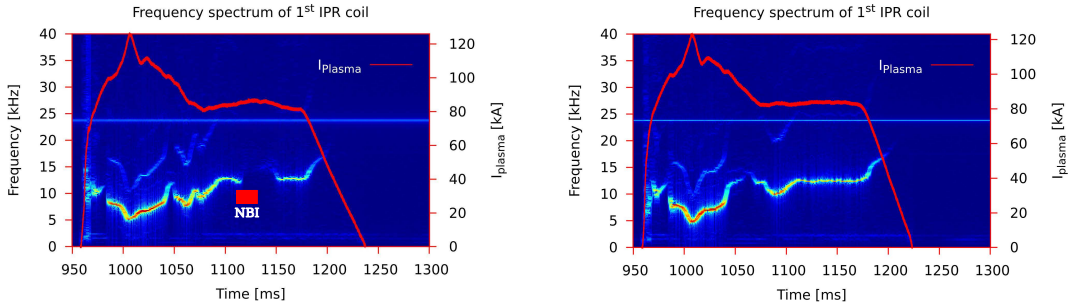

(a) (b)

Figure 5.21: Spectrograms of shots 4786 (a) and 4787 (b). Both shots have been shoot with the same parameters; however, during the shot 4786 (a) NBI have been applied.

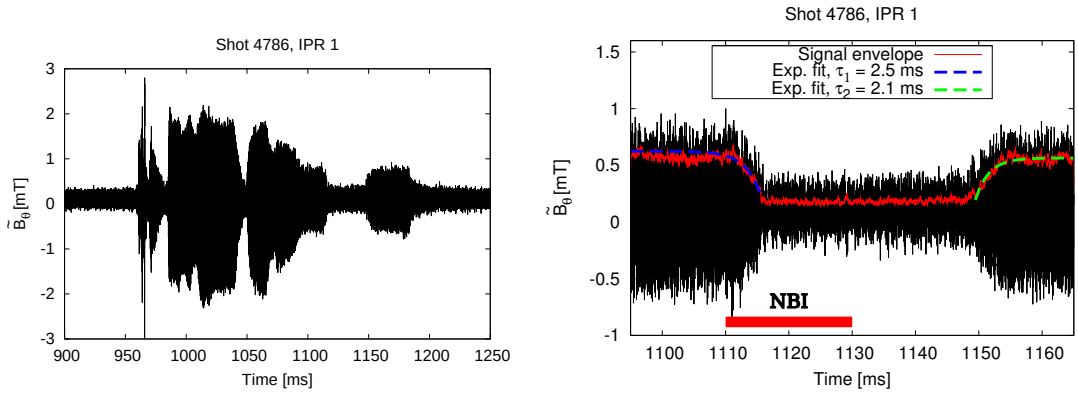

(a) (b)

Figure 5.22: (a) Magnetic perturbations measured by first IPR coil of shot 4786 and (b) the time detail of the NBI.

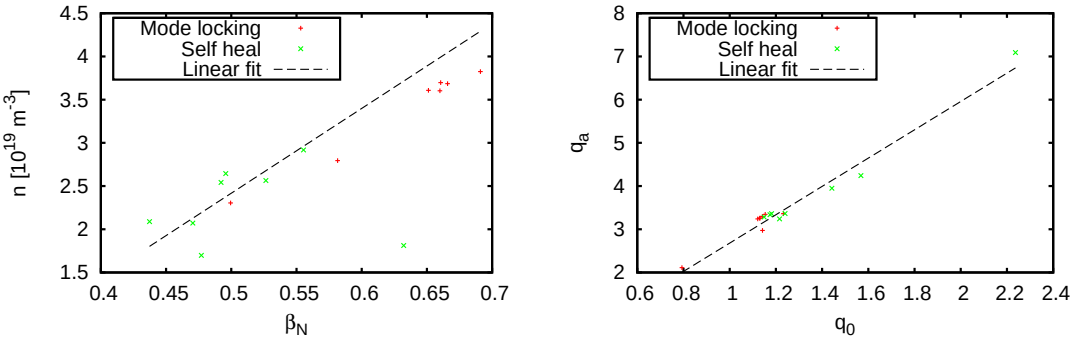

(a) (b)

Figure 5.23: (a) A plot of the plasma density as a function of a normalized β. (b) A plot of a q-edge as a function of a q in the plasma center. In the graphs is intersperse with linear fit. In the figures is clearly visible threshold between self-healed shots and mode-locked shots.

Conclusion

The goals of the present thesis can be desired into three parts. First of them deals with an overview of processes in magnetized plasma and it is presented in the first and the fourth chapters and in the first part of fifth chapter.

The introduction to problem of the magnetic confinement has been mentioned in the first chapter of the thesis. The MHD theory, which include a theory of MHD instabilities, is presented in the fourth chapter. Theory and typical behaviour of MHD instabilities have been presented in the first part of the fifth chapter. The MHD stability is introduced using the energy principle. The basic pressure driven instabilities like ballooning type modes and interchange instability are mentioned. A substantial part of the last chapter is dedicated to instabilities driven by a parallel current, namely sawtooth and tearing modes.

Second aim was concentrated on the introduction of different data processing techniques suitable for tokamak plasma.

Various data analysis techniques based on fast Fourier transform, Savitzky–Golay algorithm and Hilbert transform have been introduced, programmed and applied on data from magnetic and SXR diagnostics. The principle of various magnetic diagnostics used for measurement of tearing modes and SXR detectors used form measurement of sawtooth instability is described.

The last goal was application of the discussed techniques on the data collected on the Compass tokamak. We have used several shots to demonstrate the abilities of the diagnostics as well as different plasma instabilities.

The predicted behaviour of sawtooth instability is shown on the shot 4155. We have identified sawtooth frequency as $(400 \pm 20)\,\mathrm{Hz}$, the position of $q = 1$ rational surface and demonstrated an inaccuracy of EFIT software package in identification of q_0. The presence of Shafranov shift has been shown on the same shot.

On the chosen set of shots in Sec. 5.4.1 and 5.4.2 there has been shown a typical behaviour of tearing modes during the circularly or elliptically shaped discharges. The Mirnov instabilities during the ramp-up phase have been usually followed with tearing modes or week MHD activities during the flat top phase.

The shots have ended with disruption caused by mode locking or have ended successfully with a self-healing. The analysis of the ends of discharges is done in the Sec. 5.4.5. It has been shown that the plasma with higher values of q is more stable to disruption and the same is true for discharges with lower density and β_N.

The energy of plasma is dependant on the plasma current (throw β). As a consequence of a more free energy a faster onset of stronger tearing modes is observed (see Sec. 5.4.2).

The influence of presented tearing modes on the plasma confinement has been shown. Degradation of plasma confinement is evident the if tearing mode activity is presented.

During the shots with more stored energy, the neoclassical effect should become important and NTM should occur. However, during NBI discharges on the Compass tokamak the suppression of tearing modes has been observed. The effect of NBI has been presented in Sec. 5.4.4.

We can conclude that the goals of the thesis have been accomplished. MHD tokamak instabilities with accent to current drive sawtooth and tearing mode instabilities on the Compass tokamak have been introduced.

Based on the results of the present thesis, we can suggest a further direction for a precise analysis of MHD instabilities on the Compass tokamak.

Solving of the cylindrical tearing mode equation (5.5) can be helpful in determination of tearing modes growth on a specified rational surfaces. Technical details of solving cylindrical tearing mode equation have been mentioned in Sec. 5.3.2; however, the numerical solution of this equation has not been implemented yet. It is planed to be a future extension of the present thesis.

The signal of sawtooth instability is a typical example of non-harmonic signal. Rather than FFT, the wavelet transformation should be probably used here. Various components of the time shifted signal set can be determined by singular value decomposition (SVD). The wavelet transform and SVD are planned to be implement and applied on the signal in the near future.

Bibliography

I. T. Chapman. Controlling sawtooth oscillations in tokamak plasmas. *Plasma Physics and Controlled Fusion*, 53(1):013001, 2011. doi: 10.1088/0741-3335/53/1/013001. URL http://stacks.iop.org/0741-3335/53/i=1/a=013001.

I. T. Chapman et al. The physics of sawtooth stabilization. *Plasma Physics and Controlled Fusion*, 49(12B):B385, 2007. doi: 10.1088/0741-3335/49/12B/S35. URL http://stacks.iop.org/0741-3335/49/i=12B/a=S35.

F. F. Chen. *Introduction to Plasma Physics*. Plenum PRess, New York, 1974.

Francis F. Chen. *Introduction to Plasma Physics*. Plenum Press, New York, 1984.

B. Dudson. Magnetic confinement fusion. The University of York, 2011. URL http://www-users.york.ac.uk/~bd512/. Lecture.

J. Freidberg. *Plasma Physics and Fusion Energy*. Cambrige Uni Press, New York, 2007. ISBN 978-0-511-27375-9.

D. A. Gates et al. Neoclassical island on compass-d. *Nuclear Fusion*, 37(11):1593 – 1606, 1997.

R. J. La Haye. Neoclassical tearing modes and their control. *Phys. Plasmas*, 13 (5):055501, 2006.

C. C. Hegna and J. D. Callen. Stability of tearing modes in tokamak plasmas. *Phys. Plasmas*, 1(7):2308, 1994. doi: 10.1063/1.870628.

I. H. Hutchinson. *Principles of Plasma Diagnostics*. Cambridge Uni Press, Cambridge, second edition, 2002. ISBN 978-0-521-80389-2.

M. Imríšek et al. Observation of sawtooth oscillations in the compass tokamak. In *Week of Doctoral Students*, Prague, 2013. IPP ASCR.

B. B. Kadomtsev. Disruptive instability in tokamaks (helical plasma motions). *Soviet Journal of Plasma Physics*, 1:389 – 391, 1975.

M. Kikuchi et al. *Fusion Physics*. IAEA, Vienna, 2012. ISBN 978-92-0-130410-0.

P. Kulhánek. *Úvod do teorie plazmatu*. AGA, Praha, 2011. ISBN 978-80-904582-2-2.

J. Manickam. Stability of $n = 1$ internal modes in tokamaks. *Nuclear Fusion*, 24 (5):595, 1984. URL http://stacks.iop.org/0029-5515/24/i=5/a=006.

M. Maraschek. Control of neoclassical tearing modes. *Nuclear Fusion*, 52(7): 074007, 2012. URL http://stacks.iop.org/0029-5515/52/i=7/a=074007.

J. Mlynar et al. Introducing minimum fisher regularisation tomography to axuv and soft x-ray diagnostic systems of the compass tokamak. *Rev. Sci. Instrum.*, 83(10):10E531, 2012. doi: 10.1063/1.4738648.

M. F. F. Nave and J. A. Wesson. Mode locking in tokamaks. *Nuclear Fusion*, 30(12):2575, 1990. doi: 10.1088/0029-5515/30/12/011. URL http://stacks.iop.org/0029-5515/30/i=12/a=011.

W. Park et al. Plasma simulation studies using multilevel physics models. *Phys. Plasmas*, 6(5):1796, 1999. doi: 10.1063/1.873437.

F. Porcelli et al. Model for the sawtooth period and amplitude. *Plasma Phys. Control. Fusion*, 38:2163 – 2186., 196.

W. H. Press et al. *Numerical Recipes: The Art of Scientific Computing*. Cambrige University Press, Cambrige, 3rd edition, 2007. ISBN 978-0-521-88068-8.

A. Savitzky and M. J. E. Golay. Smoothing and differentiation of data by simplified least squares procedures. *Analytical Chemistry*, 36(8):1627–1639, 1964. doi: 10.1021/ac60214a047. URL http://pubs.acs.org/doi/abs/10.1021/ac60214a047.

E. J. Strait et al. Mhd instabilities near the β limit in the doublet iii-d tokamak. *Phys. Rev. Lett.*, 62:1282–1285, Mar 1989. doi: 10.1103/PhysRevLett.62.1282. URL http://link.aps.org/doi/10.1103/PhysRevLett.62.1282.

S. von Goeler, W. Stodiek, and N. Sauthoff. Studies of internal disruptions and $m = 1$ oscillations in tokamak discharges with soft¯x-ray tecniques. *Phys. Rev.*

Lett., 33:1201 – 1203, Nov 1974. doi: 10.1103/PhysRevLett.33.1201. URL http://link.aps.org/doi/10.1103/PhysRevLett.33.1201.

V. Weinzettl et al. Overview of the compass diagnostics. *Fusion Eng. Des.*, 86:1227, 2011. doi: 10.1016/j.fusengdes.2010.12.024. URL 10.1016/j.fusengdes.2010.12.024.

V. Weinzettl et al. Experimental evidence of neoclassical tearing modes on compass tokamak. In *40thEPS Conference on Plasma Physics*, Helsinky, 2013. IPP ASCR.

J. A. Wesson et al. *Tokamaks*, volume 1. Clarendon Press, Oxford, 2004. ISBN 0-19-8509227.

L. Zakharov et al. The theory of the early nonlinear stage of m=1 reconnection in tokamaks. *Phys. Fluids B*, 5(7):2498, 1993.

H. Zohm et al. Neoclassical mhd in asdex upgrade and compass-d. *Plasma Phys. Control. Fusion*, 1997.

List of Tables

List of Figures

List of Abbreviations

ABP	atomic beam probe
AXUV	Absolute extreme ultra-violet –Absolute X-Ray Photodiode
AXUV-(A–F)	AXUV detector on specified port (A – F)
BES	beam emission spectroscopy
DTFFT	Discrete time fast Fourier transform
ECE	electron cyclotron emission
ELM	edge localized mods
FFT	Fast Fourier transform
FT	Fourier transform
HFS	high field side
H-mode	mode of high confinement
HXR	hard X-ray
IFFT	Inverse fast Fourier transform
IPP	Institute of Plasma Physics
IPR	Internal partial Rogowski coils
LCFS	last closed flux surface
LFS	low field side
L-mode	mode of low confinement
MHD	magnetohydrodynamic
NPA	neutral particle analyser
SXR	soft X-ray